CM^2
MAGAZINE

第 74 期

创刊词

海洋是生命的摇篮，是文明的纽带。地球上最早的生命诞生于海洋，海洋里的生命最终进化成了人类，人类的文化融合又通过海洋得以实现。人因海而兴。

人类对海洋的探索从未停止。从远古时代美丽的神话传说，到麦哲伦的全球航行，再到现代对大洋的科学钻探计划，海洋逐渐从人类敬畏崇拜幻想的精神寄托演变成可以开发利用与科学研究的客观存在。其中，上个世纪与太空探索同步发展的大洋科学钻探计划将人类对海洋的认知推向了崭新的纬度：深海（deep sea）与深时（deep time）。大洋钻探计划让人类知道，奔流不息的大海之下，埋藏的却是亿万年的地球历史。它们记录了地球板块的运动，从而使板块构造学说得到证实；它们记录了地球环境的演变，从而让古海洋学方兴未艾。

在探索海洋的悠久历史中，从大航海时代的导航，到大洋钻探计划中不可或缺的磁性地层学，磁学发挥了不可替代的作用。这不是偶然，因为从微观到宏观，磁性是最基本的物理属性之一，可以说，万物皆有磁性。基于课题组的学科背景和对海洋的理解，我们对海洋的探索以磁学为主要手段，海洋磁学中心因此而生。

海洋磁学中心，简称 CM^2，一为其全名"Centre for Marine Magnetism"的缩写，另者恰与爱因斯坦著名的质能方程 $E = MC^2$ 对称，借以表达我们对科学巨匠的敬仰和对科学的不懈追求。

然而科学从来不是单打独斗的产物。我们以磁学为研究海洋的主攻利器，但绝不仅限于磁学。凡与磁学相关的领域均是我们关注的重点。为了跟踪反映国内外地球科学特别是与磁学有关的地球科学领域的最新研究进展，海洋磁学中心特地主办 CM^2 Magazine，以期与各位地球科学工作者相互交流学习、合作共进！

"海洋孕育了生命，联通了世界，促进了发展"。21 世纪是海洋科学的时代，由陆向海，让我们携手迈进中国海洋科学的黄金时代。

目录

一、研究进展

1. 南科大海洋磁学中心：南海与菲律宾海四国盆地在 20Ma 连在一起

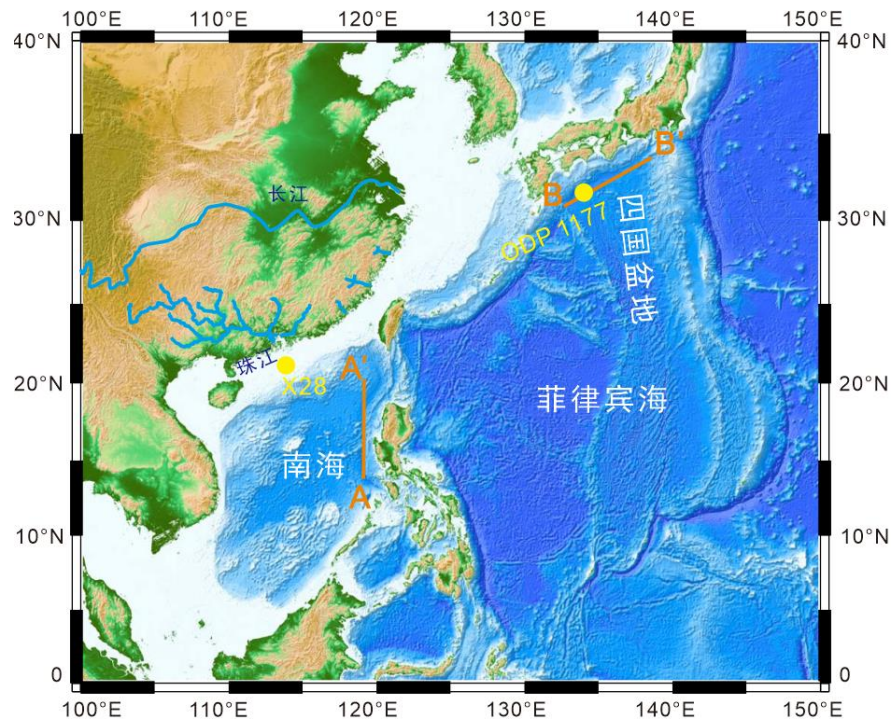南海东部长度（图 1，A-A'）和菲律宾海四国盆地北部宽度（图 1，B-B'）基本相当。南海和菲律宾海四国盆地是否可能曾连在一起呢？

图 1 南海与菲律宾海地理位置。

菲律宾海板块起源于赤道附近，并逐渐顺时针旋转和同步北向移动到现今位置。考虑到菲律宾海板块经历了由低纬度向高纬度的移动，那么必有一个时刻，其古纬度和南海的古纬度一致。

这个时间具体是什么时候？

古地磁学可以定量确定板块古纬度。板块中某一层段岩石的古纬度（λ）和该层岩石记录的古地磁倾角（I）存在定量关系（tan I = 2*tan λ）。南科大海洋磁学中心团队系统测量了菲律宾海四国盆地内大洋钻探获取的最老钻孔 ODP 1177 孔岩心的古地磁信息，得出 20 Ma 前 ODP 1177 孔的古纬度为 16.0°±4.5°N。而当时南海扩张中心的古纬度也在~16°。这为南海与菲律宾海四国盆地在地理格

1

局上曾连在一起提供了必要条件。

通过碎屑锆石对 ODP 1177 孔的物源进行了示踪。在该孔 20 Ma 前后沉积的浊流成因的砂层（图 2c）中检测出了来自珠江口的物质（图 2b），这表明南海与四国盆地在 20 Ma 前后相连通。
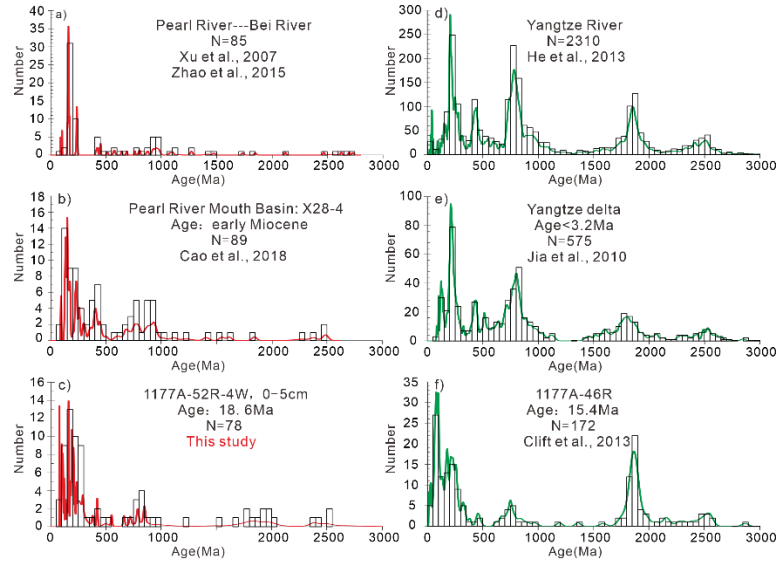

图 2 四国盆地 ODP 1177 孔获取的锆石年龄谱与潜在源区进行对比

此外，南海与菲律宾海四国盆地的形成年代相似（33/30-15 Ma），基底玄武岩均为印度洋型地幔源区成因。基于以上证据和其他地质约束，南科大海洋磁学中心团队提出南海与菲律宾海四国盆地至少在 20 Ma 就曾连在一起，共享一个扩张中心（图 3a）。而在~15 Ma，菲律宾海四国盆地与南海分离，这与南部澳大利亚与东亚的碰撞导致菲律宾海四国盆地顺时针旋转有关（图 3b）。
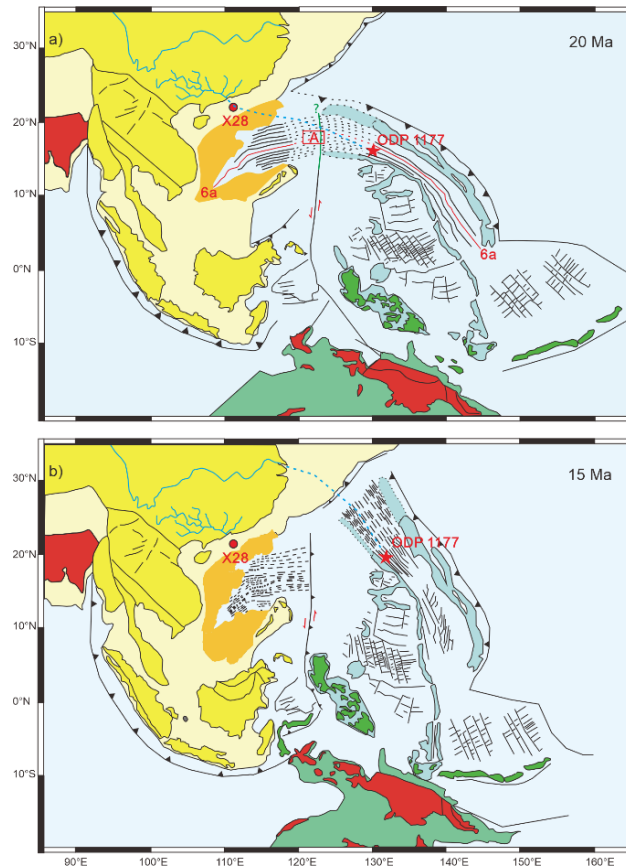
图 3 南海与菲律宾海四国盆地协同演化。（a）南海与四国盆地 20Ma 连在一起，（b）15Ma 南海与四国盆地已分离。

该研究一方面将长期认为的南海与四国盆地这两个孤立系统动态联系起来，另一方面能很好地解释"南海东部次海盆先形成，西南次海盆后形成（南海东宽西窄）；四国盆地北部先形成，南部后形成（四国盆地北宽南窄）"这一地质现象。该模型为对该区进行精细的古地磁重建和地球动力学模拟提供了基础。

南科大海洋科学与工程系博士生刘伟为本文的第一作者，南科大海洋科学与工程系刘青松讲席教授为本文的通讯作者。本论文发表在国际著名的地学领域自然指数期刊《Geophysical Research Letters》。论文连接：Liu, W., Gai, C., Feng, W., et al. (2021). Coeval evolution of the Eastern Philippine Sea Plate and the South China Sea in the Early Miocene: Paleomagnetic and provenance constraints from ODP site 1177. Geophysical Research Letters, 48, e2021GL093916. https://doi.org/10.1029/2021GL093916.

2. 单样品 IRM 曲线分解方法简介：Applying the Burr Type XII Distribution to Decompose Remanent Magnetization Curves 导读

赵翔宇

磁性矿物在自然界广泛存在，而且天然样品中通常包含来自不同物源或者成因的磁性矿物，因此识别与定量化磁性矿物的组分可以提供有力地挖掘样品的地质信息。高质量的岩石磁学测量是定量分解的前提，目前可以用来做定量分解的数据主要有磁滞回线，等温剩磁（isothermal remanent magnetization, IRM）获得曲线以及一阶反转曲线（first-order reversal curve, FORC）。其中，由于 IRM 曲线测量便捷并且解释相对容易，成为了目前定量分解中应用最为广泛的数据。Applying the Burr Type XII Distribution to Decompose Remanent Magnetization Curves 这篇文章简要回顾了 IRM 分解（IRM unmixing）这项技术，并在此基础上对方法进行了改进，极大提高了分解的自动化程度，并减少了分解过程中分析人员的主观因素对结果的影响。核心内容如下：

1. 背景介绍

如果天然样品中的不同组分之间的相互作用可以忽略，那么 IRM 曲线可以视作是各个组分的线性组合，即：

$$M^*(B) = \frac{M(B)}{M_{rs}} = \sum_{i=1}^{n} c_i M_i(B) + \varepsilon, \tag{1}$$

其中，$M^*(B)$代表用 M_{rs} 归一化的实测 IRM 曲线，$M_i(B)$则代表用来代表 n 个组分的 IRM 曲线，c_i 代表各个组分对 M_{rs} 的贡献，另外，由于测量噪音以及模型误差等因素无法拟合的部分表示为 ε。分解也可以对 IRM 曲线的导数曲线进行：

$$f(B) = \frac{dM^*(B)}{dB} = \sum_{i=1}^{n} c_i \frac{dM_i(B)}{dB} + \frac{d\varepsilon}{dB} = \sum_{i=1}^{n} c_i f_i(B) + \xi. \tag{2}$$

由于 IRM 曲线的导数，$f(B)$，代表了 IRM 随着测量场的变化，也就是反应了各矫顽力区间对 IRM 的贡献，因此也叫做矫顽力分布。相应地，$f_i(B)$ 代表了各组分的矫顽力分布。公式（1）（2）就是单样品 IRM 曲线的分解基本数学表示，而分解的关键就是选择合适的概率分布函数来模拟各个组分的 IRM 曲线（$M_i(B)$）或矫顽力分布（$f_i(B)$）。这个被用来分解的概率分布函数就叫做模型分布（model distribution）。注意，$M_i(B)$ 和 $f_i(B)$ 分别对应概率分布的累积分布函数（CDF）与密度分布函数（PDF）。

Robertson and France (1994)提出可以用对数正态分布（lognormal distribution）对样品的 IRM 曲线进行拟合。Kruiver 等人 (2001)提供了基于对数正态 CDF，使用 excel 编写的计算工具。 Heslop 等人（2002）又提供了自动化程度较高的，基于对数正态分布分解矫顽力分布曲线的可独立运行程序（IRM unmixing）。这两个计算工具的推出极大促进了 IRM 分解的应用，时至今日，对数正态分布都是最常用的模型分布。

不过，对数正态分布有一个明显的局限性。Egli （2003）和 Heslop 等人（2004）提出，自然界磁性矿物的矫顽力分布可能是非对称的，而对数正态分布则是对称的函数（因为在对数空间，对数正态就是正态分布），所以对数正态分布也许不能很充分的拟合天然样品。因为，如果某一个组分具有不对称的矫顽力分布，那么就需要一个以上的对数正态分布拟合，这样就等于人为引入了客观不存在的分量，会造成错误的解释。针对这个问题，Egli (2003; 2004a,b,c)提出了新的矫顽力分布。这个新的分布是在广义高斯分布的拓展，引入了新参数控制分布的偏度，称为 skewed generalized Gaussian distribution（SGG 分布）：

$$\text{SGG}(x, \mu, \sigma, q, p) = \frac{1}{2^{1+\frac{1}{p}}\sigma\Gamma\left(1+\frac{1}{p}\right)} \frac{\left|qe^{qx^*} + q^{-1}e^{x^*/q}\right|}{e^{qx^*} + e^{x^*/q}} \exp\left[-\frac{1}{2}\left|\ln\left(\frac{e^{qx^*} + e^{x^*/q}}{2}\right)\right|^p\right], \qquad (4)$$

SGG 分布具有极高的灵活性，可以近似的形态非常广泛。但是其数学形式非常复杂，这都给应用推广带来了影响。后来，Maxbauer 等人（2016）提出可以使用偏斜正态分布（skew normal distribution）作为 SGG 的简化，对矫顽力分布在

对数空间进行分解，并提供了具有良好用户界面的网页工具 Max Unmix。不过，该软件仍沿用传统思路，对矫顽力分布而不是 IRM 曲线进行分解。求导的问题在于测量噪音也会被放大，会对分解结果造成不利的影响。另外，选择组分个数，以及设定初始参数的过程仍然极大地依赖用户的选择，尤其当样品数量增加时，使用仍显繁琐，最终结果也不可避免地引入了人为因素。

Burr（1942）提出了一系列概率分布函数，方便使用函数的 CDF 直接拟合数据。其中第 12 种函数具有非常高的灵活性，而且具有解析的 CDF：

$$F_{\text{Burr}}(B;\alpha,\gamma,\lambda) = 1 - \left(1 + \left(\frac{B}{\lambda}\right)^{\gamma}\right)^{-\alpha}, \alpha > 0, \gamma > 0, \lambda > 0, \tag{5}$$

and

$$f_{\text{Burr}}(B;\alpha,\gamma,\lambda) = \frac{\alpha\gamma}{\lambda}\left(\frac{B}{\lambda}\right)^{\gamma-1}\left(1 + \left(\frac{B}{\lambda}\right)^{\gamma}\right)^{-\alpha-1}, \alpha > 0, \gamma > 0, \lambda > 0, \tag{6}$$

本文系统考察了 Burr 第 12 类函数作为模型分布拟合 IRM 曲线的可行性，并分析了影响单样品 IRM 分解的两个重要因素，分别为测了噪音以及分解参数的选择。

2. 主要结果

2.1 Burr 分布与 SGG 分布的对比

通过使用 SGG 函数作为模型分布分解天然样品，Egli（2004a）给出了一些有代表性的组分的矫顽力分布（图 1a 彩色曲线）。这些分布都可以近似地使用 Burr 函数拟合。同样，对于 SGG 分布也可以近似各种 Burr 分布的形态。这表明，在实际应用层面，Burr 分布与 SGG 分布有很高的近似度。
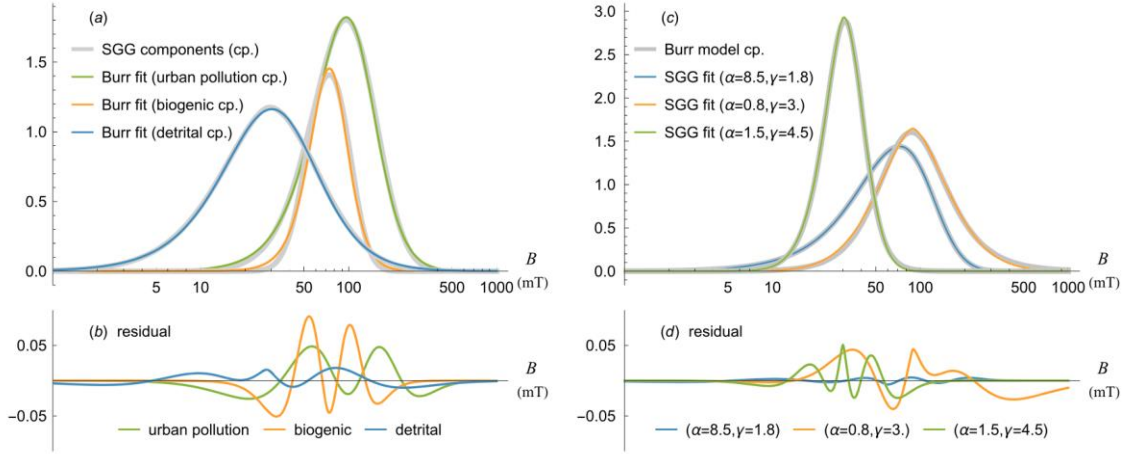
图 1：SGG 分布与 Burr 分布的比较。Comparison between the Burr type XII distribution and the skewed generalized Gaussian (SGG) distribution. (a) The SGG components (gray lines, from Egli (2004a)) and best fits of the Burr type XII distributions (colored lines) with the following shape parameters (α, γ): detrital cp ($\alpha = 1.517$, $\gamma = 1.806$), biogenic cp ($\alpha = 1.446$, $\gamma = 4.568$), and urban pollution cp ($\alpha = 2.055$, $\gamma = 2.657$). (b) Corresponding residuals. (c) Best fits of the SGG distribution (colored lines) to the modeled Burr components (gray lines). Shape parameters for modeled components are shown in legends. (d) Corresponding residuals. Note that cp means component.

3.2 测量噪音以及参数选择对于分解结果的影响

测量噪音是 IRM 分解过程中的一个敏感因素，对于基于 Burr 函数的分解也不例外。当测量噪音存在的时候，数值模拟的例子表明，分解得到的组分通常会偏离真实组分（图 2a，即原文图 4a）。噪音程度增加时，偏离程度通常更加显著（图 2e）。另外，对于同一组数据，如果直接对 IRM 曲线进行拟合，得到的结果会比对矫顽力分布曲线拟合好（图 2c），就是因为求导过程放大了噪音。当组分的个数增加时，分解对噪音更加敏感。比如，当组分增加到 3 个时，而测量噪音与图 2a 中数据一样，复原的组分的偏离程度更加明显（图 2g）。这一现象对于基于其他模型函数的分布也同样适用（图 3，即原文图 5）。另外，IRM 分解的初始工作中，需要设定初始参数，包括组分的个数，每个组分的参数。由于 IRM 分解的 本质是对数据的非线性的拟合（公式 1，2），所以算法寻找到的最优解依赖初始参数，并且很有可能结束于局部最小值，而不是全局最小值，因此 IRM 分解具有多解性。图 3c 就以 SGG 函数为例，展示了这样的

情况，当选择不同参数作为初始值时，得到了蓝色实线与虚线代表的两种不同的分解结果。

以上例子表明，用于 IRM 分解的数据，最好具有尽可能高的信噪比。为此，IRM 曲线应该视为优于矫顽力分布曲线的选择，因为后者不可避免地放大了测量噪音。
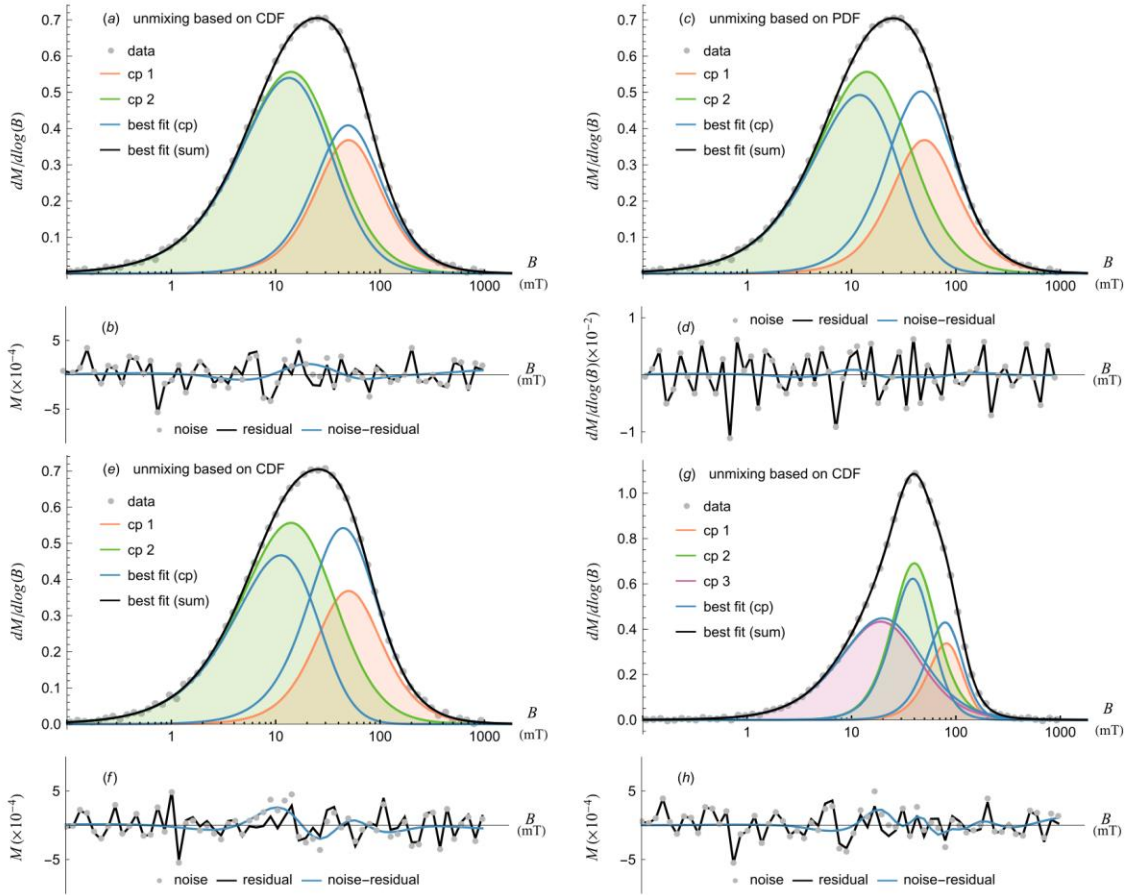

图 2：测量噪音对于基于 Burr 函数的 IRM 分解的影响。The component analysis of noisy data. (a) The modeled data (dots) consist of two Burr type XII components (cp1 and cp2, shown as green and orange curves) and noise. The estimated components and the sum are shown in blue and black lines, respectively. Note that the analysis is based on the cumulative form of the mixture model. (b) The residual of the analysis (black) versus the modeled noise (dots). The blue line indicates the difference between the residual and modeled noise. (c and d) Same as (a) and (b) except that the analysis is performed on the coercivity distribution using the probability distribution function (PDF)

form of the mixture model. (e and f) Same as (a) and (b) except that the modeled noise is different. (g and h) The case with 3 modeled components. The modeled noise is the same as that used in (a).
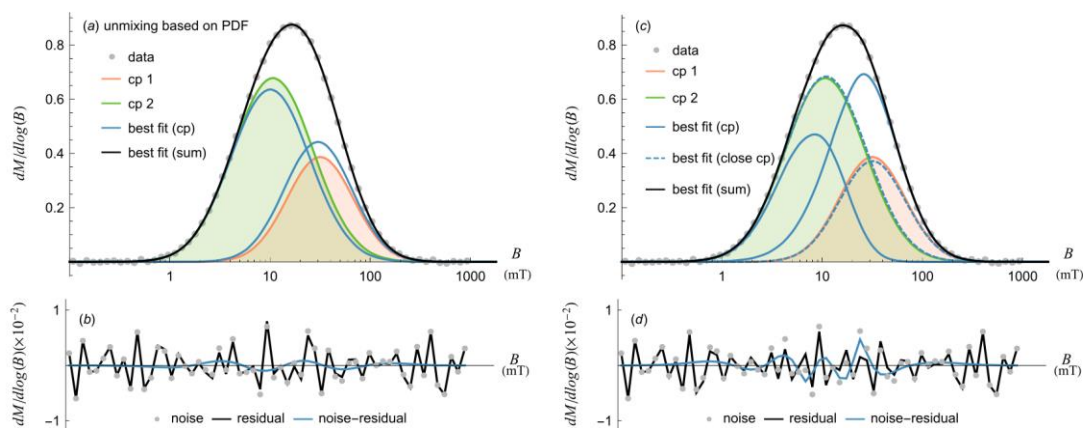

图 3: 测量噪音对于基于对数正态及 SGG 函数的 IRM 分解的影响。Component analysis using the normal and skewed generalized Gaussian distributions. (a) The modeled data (dots) consist of two normal components (cp1 and cp2, shown as green and orange curves) and noise. The best fit com- ponents and the sum are shown in blue and black lines, respectively. (b) The residual (black) versus the modeled noise (dots). The blue line indicates the difference between the residual and the noise. (c) Results based on the SGG distribution. The data are the same as that shown in (a). The solid blue lines and dashed lines indicate results with two different sets of initial guesses. (d) The residual (black) corresponds to the results shown in solid blue lines in (c).

2.3 使用 Burr 函数分解实际样品

Burr 函数可以很好地拟合实际样品的 IRM 曲线。图 4 和图 5（即原文图 6 和 7）分别展示了利用对数正态，SGG 和 Burr 函数作为模型分布对合成磁铁矿以及蛇纹岩化的橄榄岩的分解结果。由于实验室合成的磁铁矿是在恒定条件下生成的，应该只具有一个组分。然而，采用 1 个对数正态组分并不能很好地拟合测量数据，尤其是低矫顽力一端的偏差更加明显。不过，SGG 和 Bur 函数都可以叫充分地对数据进行拟合（图 4a）。这表明，和 SGG 一样，Burr 函数的灵活性可能更适合于模拟实际样品的组分。通常，单样品 IRM 分解可以通过增加组分个数

来提升拟合效果。图 4b 展示了双组分的分解结果。可以看到，拟合残差显著降低（图 4d）。然而，使用不同的模型分布得到的组分却并不一致（图 4b）。这意味着，双组分的假设可能欠缺合理性。因此，尽管单组分的拟合效果稍差，但是却与现实情况更为接近，即该合成磁铁矿样品只具有一个组分。
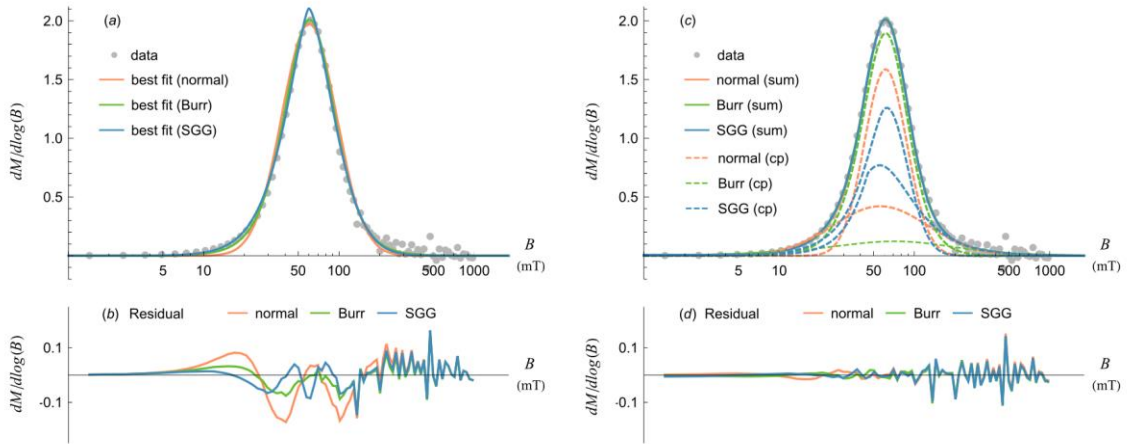

图 4：Component analysis of synthetic magnetite. (a) Results of component analysis using a single component. The raw data are shown as dots. The best fits of the normal, Burr type XII, and SGG distributions are shown in orange, green, and blue curves, respectively. The Burr component is characterized with α = 1.085, γ = 3.407 and λ = 62.293 mT. (b) Residuals. (c) Results of component analysis using two components. Color codes are the same as in (a). Individual components are shown as dashed lines. Sums are shown as solid lines. (d) Residuals.

蛇纹岩化是洋壳常见的热液反应。蛇纹岩化程度较高的橄榄岩中通常富含磁铁矿。图 5 是对一块蛇纹岩化程度达到 96% 的样品分解的结果。可以看到，热液过程形成的磁铁矿与实验室合成的磁铁矿有着类似的矫顽力分布。一个 Burr 或 SGG 组分都可以充分地拟合数据。对数正态组分在低矫顽力端仍然有拟合不足。使用双分量分解的话，可以从拟合残差看出（图 5d），三种分布整体拟合的效果非常相似。而且三种结果得到的组分也具有一定程度的相似性，尤其是使用 Burr 分布和 SGG 分布得到的组分，非常相似。这样的结果意味着，磁铁矿有一定的可能
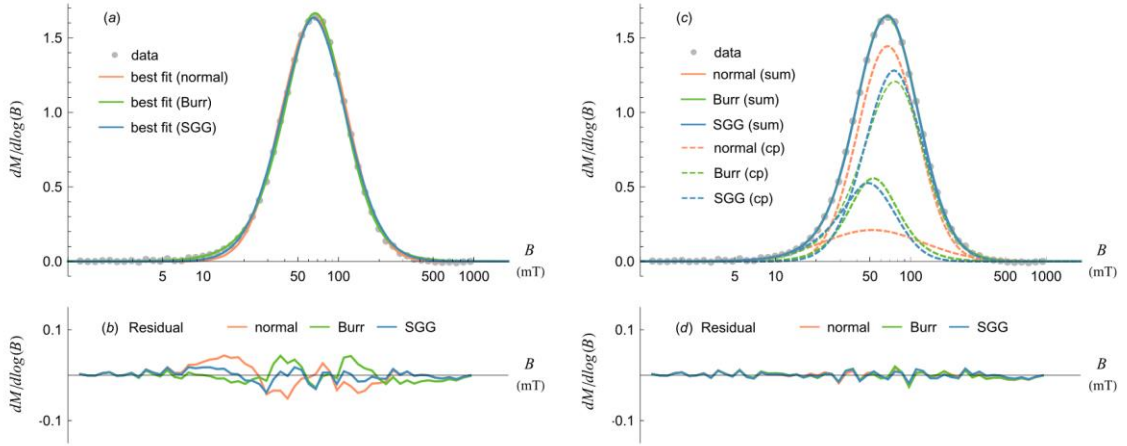
性是分两个阶段形成的。但是，若要验证这一点，岩石学以及地化证据是非常必要的。

图 5: Component analysis of serpentinized peridotite. (a) Results of component analysis using a single component. The raw data are shown as dots. The best fits of the normal, Burr type XII and SGG distributions are shown in orange, green, and blue curves, respectively. The parameters for the Burr component are α = 1.244, γ = 2.721, λ = 72.872 mT. (b) Residuals. (c) Results of component analysis using two components. Color codes are the same as in (a). individual components are shown as dashed lines. The sums are shown as solid lines. (d) Residuals.

3. 讨论

3.1 模型分布选择

单样品 IRM 分解的重要基础就是假设可以选择一个合适的模型分布近似真实的组分。但关于什么分布是合适的，目前是没有理论基础的，只能基于经验。在 SGG 分布出现之前，对数正态是唯一选择；而 SGG 也长期作为唯一的可以表示非对称分布的模型分布使用。不过，随着 skew normal 和 Burr 分布的引入，研究模型分布的选择对于分解的影响成为可能。很显然的是，由于后三者分布都能比对数正态分布更好地拟合偏态分布，比如这些分布通常可以更好地拟合低矫顽力部分（图 4，5），因此使用更灵活的分布分解样品有助于减少虚假组分的出现。当然，在某些情况下，灵活的分布可能也会掩盖某些真实存在组分。比如，Egli（2003）展示了一个 SGG 分布能够近似拟合两个高度重叠的对数正态分布的组合。归根

11

结底，还是需要通过拟合真实端元来评价哪种分布更合适。但这不是一件容易的工作，因为自然界的纯端元通常是很难获取的。

3.2 单样品 IRM 分解的多解性

由于 IRM 分解的本质是求解非线性函数的最优解，在定义域范围内存在很多局部极小值。受参数初始值影响，计算通常会终结在不同的极小值，这是造成多解性的根本原因。传统软件依赖人工选择初始参数，既繁琐又增加了主观因素。与其如此，不如讲参数选择的过程自动化。首先，可以利用 AIC 等统计量确定最优的组分个数。之后，可以用程序随机生成各个组分的初始参数，并对数据进行分解。在进行过 n 次这样的分解过程后，选出其中拟合残差最小的结果作为最优解。当 n 足够大的时候，结果应该更接近于全局最优解。这一自动化流程极大提高了分析的效率和客观性。

不过，需要指出的是，当数据中包含测量噪音时，分解的全局最优值并非时最接近真实情况的解。图 3c，d 表示了这一情况。虚线对应的解，更接近真实组分，然而其对应的拟合残差却更大一些。这是因为，测量噪音的存在改变了目标函数在参数空间的形态，所以各个极小值在参数空间的位置也相应地改变了。这说明了噪音的存在对分解是有非常不利的影响的，因此应该尽量压制。也是因为这个原因，测量 IRM 曲线时应尽可能地提高信噪比，分解时应该尽可能地使用 CDF 形式，而不是 PDF 形式。不过由于测量噪音是无法避免的，建议实际操作时，多次测量，对平行数据进行分解，观察结果是否一致。这样可以对分解结果的多解性有一个大致的估计。

3.3 模型分布于残差

如果拟合残差只是源自测量噪音，则其应该具有随机形状。如果拟合残差的形状出现近似规律的波形，如图 1b，d 所示，则意味着以下三种情况。首先，如果分解选择的组分个数与实际组分个数一致，则原因是模型分布与真实组分存在差异。或者是，分解选择的组分个数小于实际分量造成的欠拟合。第三种情况是前两种情况同时出现。无论哪种情况，提高分解的组分个数都可以降低拟合残差。

关于判断选择的组分个数是否合理，建议使用统计量作为客观的判断。AIC（Akaike Information Criterion）是本文使用的统计量，可以用来判断最优的组分个数。当然，鉴于模型分布与真实组分还存在不确定性，建议将利用统计量判断出的最优组分个数作为一个上限，即实际存在的组分个数是有可能小于这个最优值的。这在分解合成磁铁矿的例子里有所体现（图 4）。最优解是 2 个组分，但实际样品有可能只有 1 个组分。

3.4 控制噪音的影响

减少噪音有助于提高 IRM 分解的质量。除了测量上的措施，数据平滑，滤波，以及尽量使用 IRM 曲线进行分解之外，还有一个可以尝试的方案，即对数据进行过拟合。如图 4，5 所示，通过增加分量个数，拟合模型可以尽可能逼近曲线上的细节。这与多项式拟合是一个道理。不同的是，模型分布不能灵活地适应随机噪音，因此这种过拟合会压制噪音。由于现在至少有四种可以分解 IRM 的模型分布，完全可以选择一种模型分布对数据进行过拟合从而降低噪音，然后选择其他的模型分布对降噪后的数据分解。

4. 结伦

Burr 分布是一种灵活的概率分布函数，并且具有解析的 CDF 形式，可以方便地用于分解 IRM 曲线和矫顽力分布曲线。从实际应用角度，Burr 与 SGG 分布有接近的效果，但由于 Burr 具有 CDF 形式，可以避免对数据求导，从而减少了测量噪音对分解的不利影响。

受到测量噪音以及参数选择等因素影响，单样品的 IRM 分解具有多解性，在实际应用过程中要注意。用户在测量 IRM 曲线时，建议尽量提高信噪比。另外，本文提出了自动化的分析流程，可以极大提高分析效率以及客观性。基于这个改进，在分解 IRM 时，分析人员可以更高效和充分地利用多种模型分布。比如，作为一种评估分解合理性的途径，可以对比不同分布得到的结果是否有可比性。

二、文献速递

1. 过去 260 千年南大洋中太平洋与大西洋断面风尘粒度呈现相反模式

翻译人：仲义 zhongy@sustech.edu.cn

摘要： 沉积物粒度范围在（2-10 um）可以有效地反映在冰期-间冰期尺度上风力强度和源区特征。然而，到目前为止，我们对南大洋冰期-间冰期粉尘颗粒大小的变化知之甚少，这可能与南半球西风强度与位置的变化有关。在此基础上，作者分析南大洋太平洋（PS75/056-1）和大西洋（ODP Site 1090）亚南极深海沉积物粒度分布。在两个南大洋断面上发现粉尘颗粒大小呈现相反的趋势。冰期时太平洋断面区粒度更粗，而在大西洋断面粒度更细。而在南太平洋，更高的风尘平均粒径与冰期铁通量变化较为一致。相反，在南大西洋地区，冰期铁输入对应于冰期平均风尘粒度降低，与南极冰心记录较为一致。我们的结果说明相反的粒度趋势变化是由于冰期风尘来源及风力搬运模式的不同响应有关。比如在南太平洋地区，作者认为澳大利亚上空的风强度增强，使得更大的风尘颗粒得以释放。这种增强意味着西风带向北移动，从而促使来自澳大利亚和新西兰的粉尘的输送。而对于大西洋地区，冰期风尘粒度见效可能是由于巴塔哥尼亚冰川活动增强，导致暴露在大陆架的更多细粒风尘搬运到南大西洋。这些发现表明，需要更加广泛地研究南大洋的风尘沉积物特性，这样可以为西风向南大洋输送的来源和变化模式提供时间和纬度范围方面的指示。

ABSTRACT: Downcore sediment grain-size records of mineral dust (2-10 mm) can provide key insights into changes in wind strength and source-area characteristics over

glacial-interglacial timescales. However, so far, little is known about glacial-interglacial changes of dust grain size in the open Southern Ocean, which are potentially associated with changes in the strength and position of the southern westerly winds. Here, we analyzed the grain-size distributions of subantarctic deep-sea sediments from the Pacific (PS75/056-1) and Atlantic (ODP Site 1090) sectors of the Southern Ocean, downwind of the major Southern Hemisphere dust source regions. Dust mean grain sizes show opposite trends in the two Southern Ocean sectors. Larger glacial grain sizes are observed in the Pacific sector, while finer glacial grain sizes are observed in the Atlantic sector. In the South Pacific, larger mean dust grain sizes parallel higher Fe fluxes during glacials. In contrast, in the South Atlantic record increased glacial Fe fluxes coincide with a decrease in glacial mean dust grain sizes consistent with some Antarctic ice core records. Our results suggest that the opposing grain-size trends are the result of different responses to glacial conditions in the sources and of changing wind and transport patterns. For the South Pacific, a possible explanation of our results could be an intensification of wind strength over Australia enabling emission of larger dust particles. This strengthening would imply a northward shift of the westerlies which facilitated the transport of dust from enhanced and/or more Australian and New Zealand sources. For the Atlantic, the decreased glacial dust grain size could be the consequence of increased glacial activity in the Patagonian Andes, generating and supplying more and finer-grained dust from the exposed continental shelf to the South Atlantic. These findings indicate that more extensive studies of wind-blown sediment properties in the Southern Ocean can provide important insights on the timing and latitudinal extent of climatic changes in the sources and variations of transport to the Southern Ocean by the westerly winds.
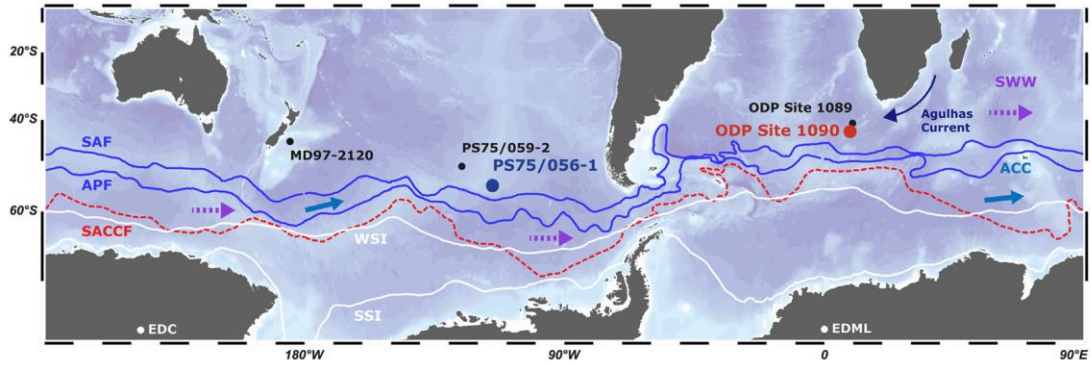
Figure 1. Map of the Southern Ocean with core locations PS75/056-1 (blue) and ODP Site 1090 (red), and referenced ice- and sediment cores. Colored lines refer to mean positions of major front systems (Orsi et al., 1995). SAF: Subantarctic Front, APF: Antarctic Polar Front. SACCF: Southern Antarctic Circumpolar Current Front. Mean extension of winter and summer sea ice (WSI and SSI) are indicated by white lines (Comiso, 2003). Arrows indicate the flow direction of the Antarctic Circumpolar Current (ACC; blue), Agulhas Current (dark blue) and the direction of the Southern Westerly Winds (SWW; purple). The map was generated using Ocean Data View (Schlitzer, 2018). (For interpretation of the references to color in this figure legend, the reader is referred to the Web version of this article.)
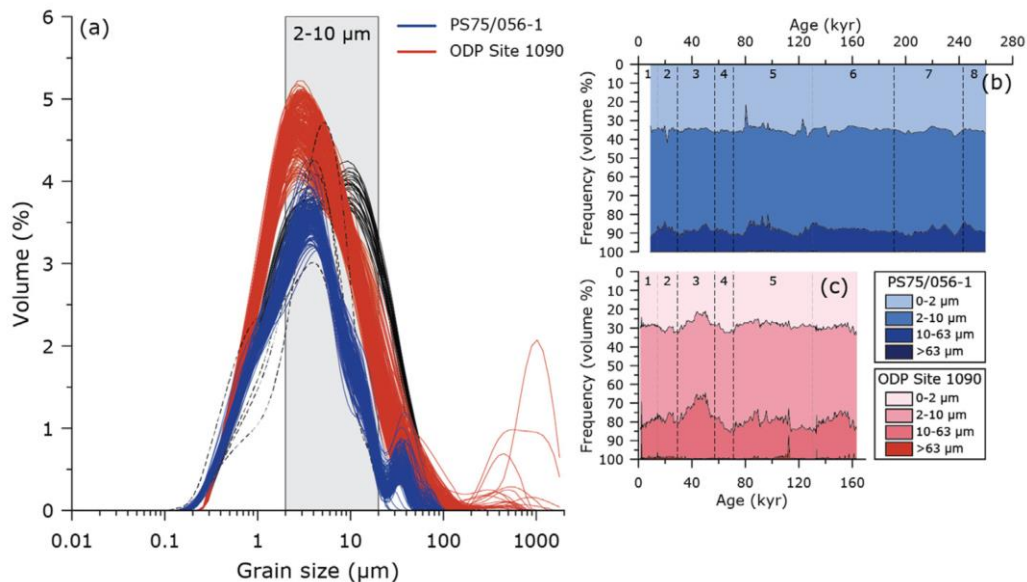

Figure 2. A: Grain-size distributions of terrigenous sediments of PS75/056-1 (blue) and ODP Site 1090 (red). Each line represents a single sample. For PS75/056-1, grain sizes were measured on the <63 mm fraction. The black lines represent outliers (PS75/056-1, dashed lines) and MIS3 samples

(ODP Site 1090, solid lines). The grey bar marks the assumed dust (2-10 mm) fraction. B & C: Composition of standard size fractions for sediments of PS75/056e1 (B) and ODP Site 1090 (C), versus age. Dashed lines and numbers at the top indicate the Marine Isotope Stages. (For interpretation of the references to color in this figure legend, the reader is referred to the Web version of this article.)
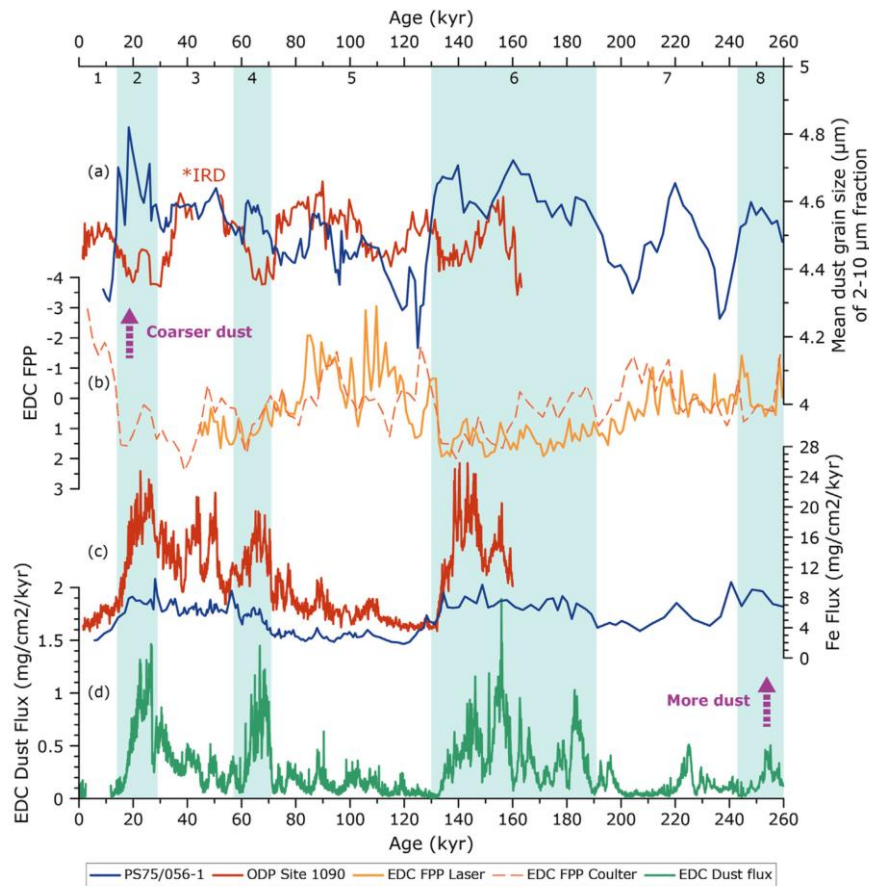

Figure 3. A: Mean grain size (2-10 mm fraction) of sediments of PS75/056-1 in the Pacific sector of the Southern Ocean (blue) and ODP Site 1090 in the Atlantic sector (red). Grain sizes for ODP Site 1090 during MIS 3 are omitted as they likely represent an alternative sediment source, as well as four coarse outliers of PS75/056e1 (displayed in Fig. S2). B: Fine Particle Percentage (FPP; percentage of particles between 1 and 2 mm) of EDC ice core inferred by both laser particle sizer (solid line) and Coulter Counter (dashed line), where smaller values correspond to coarser-grained dust (both from Lambert et al., 2008). C: Fe flux in sediments of core PS75/056-1 (blue; Lamy et al., 2014) and ODP Site 1090 (red; Martínez-García et al., 2014), representing dust deposition. D: EDC dust flux (Lambert et al., 2012). Both EDC records are plotted on the most recent AICC2012

chronology (Veres et al., 2013). Marine Isotope Stages are indicated at the top, with blue bars highlighting glacial conditions. (For interpretation of the references to color in this figure legend, the reader is referred to the Web version of this article.)

2. Hikurangi 高原俯冲是西南太平洋 Vitiaz 弧裂解和 Havre 海槽打开的触发器

翻译人：冯婉仪 fengwy@sustech.edu.cn

摘要：Vitiaz 弧的裂解形成了西南太平洋的 Tonga-Kermadec 洋脊和 Lau-Colville 洋脊，这两个洋脊之间被北部的 Lau 盆地和南部的 Havre 海槽分隔开。我们展示了延伸~ 900 km 至新西兰北部的 Kermadec 洋脊和 Colville 洋脊（36° S - 28° S）的新的微量元素和 Sr-Nd-Hf-Pb 同位素地球化学数据。这是为了（1）将残余弧的成分与第四纪 Kermadec 弧火山活动进行比较；（2）限定残余弧地球化学成分的空间变化；（3）评估 Hikurangi 火成岩高原的俯冲作用对早期弧熔岩地球化学的影响；以及（4）阐明什么原因可能导致弧裂解。与 Kermadec 洋脊相比，Colville 洋脊具有更高的较高不相容不活动元素与较低不相容不活动元素比值和较大的同位素比值重叠，与 Vitiaz 弧后较富集的上地幔发生低程度熔融成因相一致。在 ~8-3 Ma 之间，与较古老和较年轻的弧熔岩相比，弧的两侧（~36° S - 29° S）具有更富集的（EMI 型）成分（较低的 $^{206}Pb/^{204}Pb$ 和 $^{207}Pb/^{204}Pb$，较高的 Δ8/4 Pb 和 $^{87}Sr/^{86}Sr$）。曾经与 Hikurangi 高原连接的 Manihiki 高原的高钛玄武岩可能成为 Vitiaz 弧的富集端员。我们认为，仅从活动元素的同位素比值来看，富集的高原特征是通过来自俯冲的 Hikurangi 高原的西缘或 Hikurangi 高原碎片的含水流体传输至上覆地幔楔。我们的结果表明高原俯冲引起了弧裂解和弧后张开。

ABSTRACT: Splitting of the Vitiaz arc formed the Tonga-Kermadec and Lau-Colville Ridges (southwestern Pacific Ocean), separated by the Lau Basin in the north and Havre Trough in the south. We present new trace element and Sr-Nd-Hf-Pb isotope geochemistry for the Kermadec and Colville Ridges extending ~ 900 km north of New Zealand (36°S - 28°S) in order to (1) compare the composition of the arc remnants with Quaternary Kermadec arc volcanism, (2) constrain spatial geochemical variations

in the arc remnants, (3) evaluate the effect of Hikurangi igneous plateau subduction on the geochemistry of the older arc lavas, and (4) elucidate what may have caused arc splitting. Compared to the Kermadec Ridge, the Colville Ridge has higher more-incompatible to less-incompatible immobile element ratios and largely overlapping isotope ratios, consistent with an origin through lower degrees of melting of more enriched upper mantle in the Vitiaz rear arc. Between ca. 8 and 3 Ma, both halves of the arc ($\sim 36\,°S$ - $29\,°S$) included a more enriched (EM1-type) composition (with lower $^{206}Pb/^{204}Pb$ and $^{207}Pb/^{204}Pb$ and higher $\Delta8/4$ Pb [deviation of the measured $^{208}Pb/^{204}Pb$ ratio from a Northern Hemisphere basalt regression line] and $^{87}Sr/^{86}Sr$) compared to older and younger arc lavas. High-Ti basalts from the Manihiki Plateau, once joined to the Hikurangi Plateau, could serve as the enriched Vitiaz arc end member. We propose that the enriched plateau signature, seen only in the isotope ratios of mobile elements, was transported by hydrous fluids from the western margin of the subducting Hikurangi Plateau or a Hikurangi Plateau fragment into the overlying mantle wedge. Our results are consistent with plateau subduction triggering arc splitting and backarc opening.
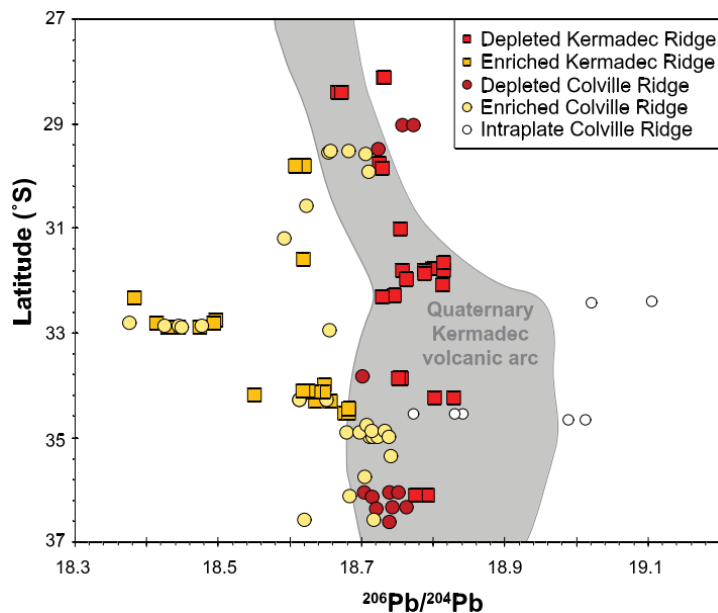

Figure 1. Plot of $^{206}Pb/^{204}Pb$ versus latitude, showing a peak in enrichment (lowest $^{206}Pb/^{204}Pb$) at 33° S. One degree of latitude has been added to Colville Ridge samples to correct for the opening of the Havre Trough.
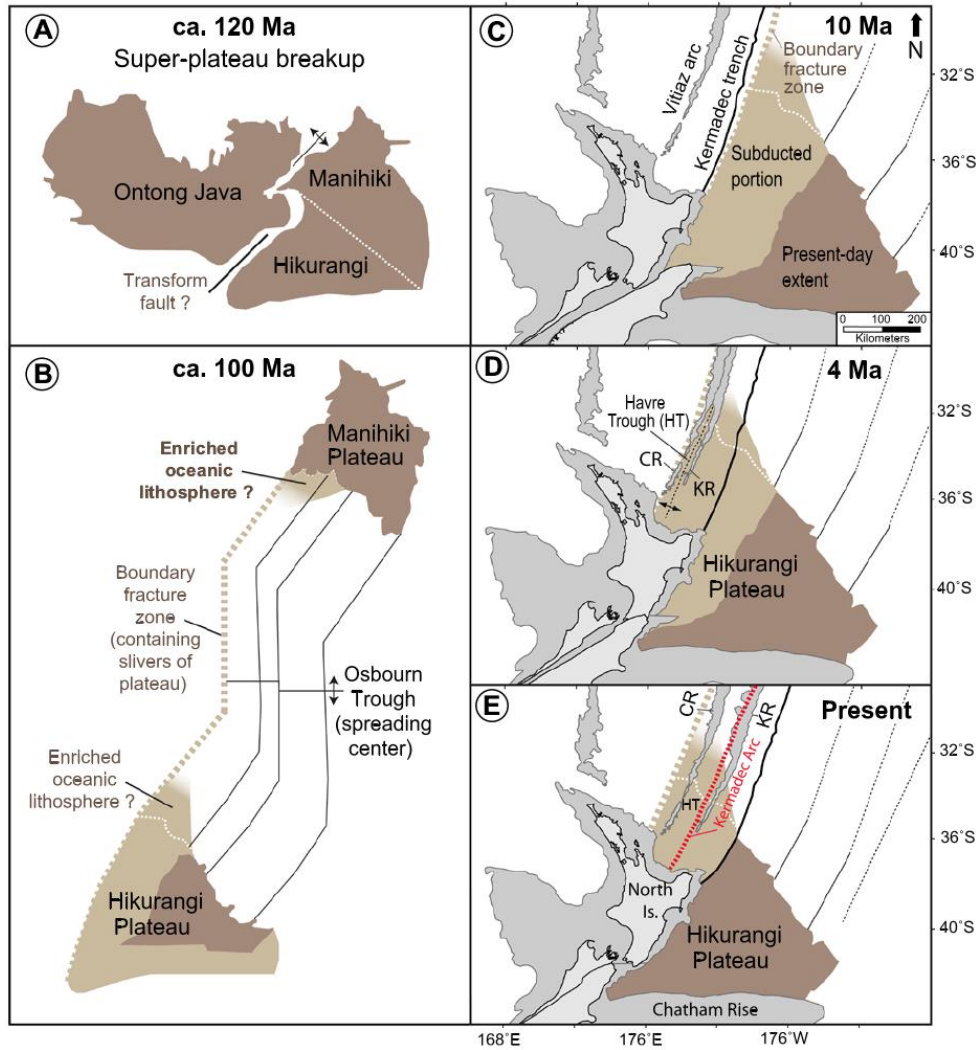
Figure 2. Model to explain the presence of enriched signal in Kermadec Ridge and Colville Ridge lavas between ca. 8 and 3 Ma. (A) At ca. 120 Ma, Ontong Java rifts away from the Manihiki + Hikurangi plateau fragment. (B) At ca. 117-97 Ma, spreading along the Osbourn spreading center creates ~3000 km of seafloor between Manihiki and Hikurangi (Mortimer et al., 2019). Some oceanic lithosphere formed near rifted margins of plateau fragments may also have enriched plateau-like composition. At ca. 105 Ma, Hikurangi collides with the Gondwana subduction margin, which later becomes the Chatham Rise of Zealandia. (C) At ca. 10 Ma, the western margin of Hikurangi is just outboard of the Kermadec-North Island (New Zealand) trench. (D) From ca. 8 to 3 Ma, the western Hikurangi margin subducts beneath the Vitiaz arc, which splits into Colville Ridge (CR) and Kermadec Ridge (KR), forming the Havre Trough. (E) Present configuration. (Modified from Davy et al., 2008; Timm et al., 2014.)

3. 地球上第一次氧化还原演变

翻译人：李园洁 liyj3@sustech.edu.cn

摘要：大气和海洋中分子氧的升高是地球历史最重要变化之一。目前大部分的研究集中于接近元古代开始的大氧化事件（GOE），在这之后氧气不可逆转升高，占据大气的超过 0.1%。很多证据表明在太古代末期（25 亿年前）之前发生了一个更小的氧化事件。另外，有证据发现在整个太古代是轻微的氧化环境。这个新出现的证据表明以具有两个或更多早太古代氧化事件为特征的地球系统的第一次氧化还原演变中 GOE 可能是顶极。理解这次演变的时间和速度是揭示地球演化驱动力的关键，对寻找地球之外的生命具有重要意义。

ABSTRACT： The rise of molecular oxygen (O_2) in the atmosphere and oceans was one of the most consequential changes in Earth's history. While most research focuses on the Great Oxidation Event (GOE) near the start of the Proterozoic Eon-after which O_2 became irreversibly greater than 0.1% of the atmosphere-many lines of evidence indicate a smaller oxygenation event before this time, at the end of the Archean Eon (2.5 billion years ago). Additional evidence of mild environmental oxidation-probably by O_2-is found throughout the Archean. This emerging evidence suggests that the GOE might be best regarded as the climax of a broader First Redox Revolution (FRR) of the Earth system characterized by two or more earlier Archean Oxidation Events (AOEs). Understanding the timing and tempo of this revolution is key to unraveling the drivers of Earth's evolution as an inhabited world-and has implications for the search for life on worlds beyond our own.
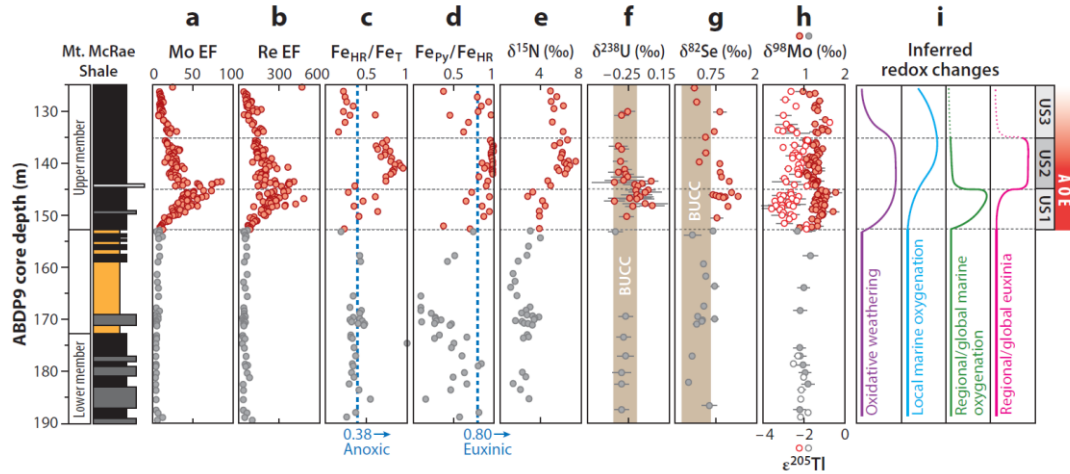
Figure 1. Many geochemical trends in the upper member of the Mt.McRae Shale indicate that Earth experienced an AOE at ~2.5 Ga. Of note, EFs have been recalculated in panels *a* and *b* relative to bulk upper continental crust values (Rudnick & Gao 2003). The blue dashed lines in panels *c* and *d* signify cutoffs, at or above which local deposition can be confidently characterized as anoxic and/or euxinic, respectively (Raiswell et al. 2018). The brown rectangles in panels *f* and *g* signify BUCC values referenced in those isotope studies. Similar to Ostrander et al. (2020), we have split the US member into three geochemically distinct intervals: US1, US2, and US3. Abbreviations, AOE, Archean Oxidation Event; BUCC, bulk upper continental crust; EF, enrichment factor; Fe$_{HR}$, highly reactive iron; Fe$_{Py}$, pyrite iron; Fe$_T$, total iron; US, upper shale. All data are from shale samples preserved in Agouron drill core ABDP9. Data for panels *a* and *b* from Anbar et al. (2007), panels *c* and *d* from Reinhard et al. (2009), panel *e* from Garvin et al. (2009), panel *f* from Stüeken et al. (2015a), panel *g* from Kendall et al. (2013), and panel *h* from Duan et al. (2010) and Ostrander et al. (2019).
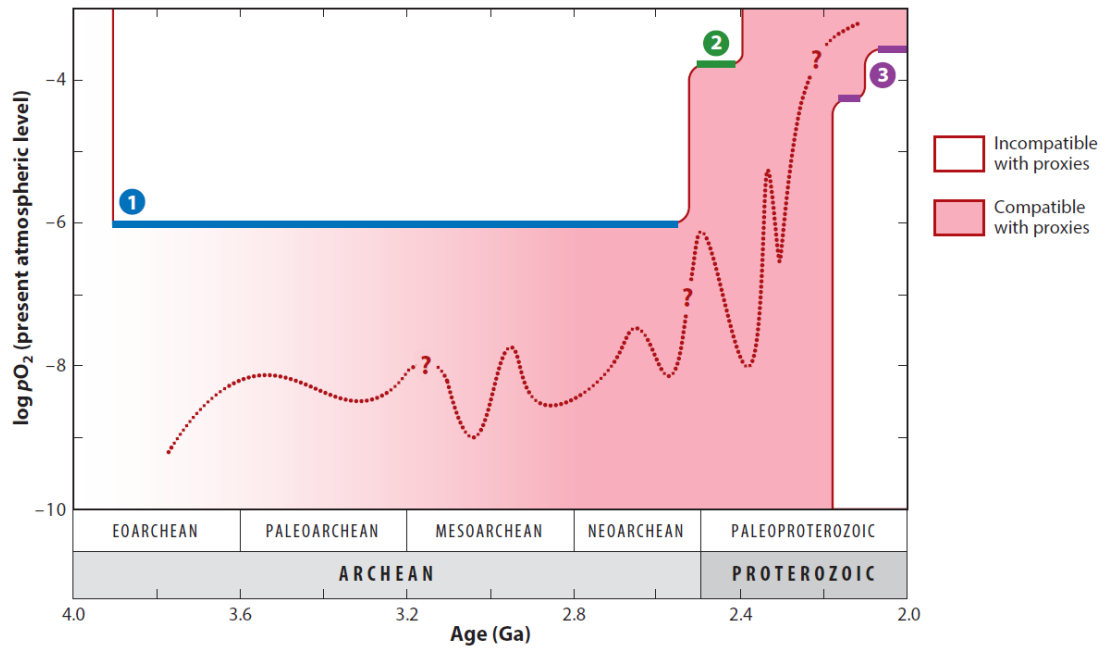
Figure 2. Hypothetical Archean atmospheric pO_2 curve. Quantitative constraints provided by MIF-S [❶; blue (Catling & Zahnle 2020)] and detrital pyrite and uraninite grains [❷; green (Johnson et al. 2014)] set pO_2 upper limits at different times during the Archean Eon. Lower limits for Paleoproterozoic pO_2 have been inferred from paleosol geochemistry [❸; purple (Kanzaki & Murakami 2016)]. Estimating lower limits for Archean pO_2 is complicated by the fact that, because O_2 was a trace gas for most, if not all, of this time, pO_2 may have varied both spatially and temporally. Abbreviations: MIF-S, mass-independent fractionation of S isotopes; PAL, present atmospheric level; pO_2, molecular oxygen partial pressure.

4. 基于相关性的历史时期古地磁场快照模型

翻译人：柳加波 liujb@sustech.edu.cn

摘要：针对时间静止的全球地磁场，本文提出了一个新的建模概念。利用贝叶斯非参数方法提供了与现实位置相关的不确定性估计。通过很少的主观先验假设来系统处理与建模相关的变量。本文采用了泛函分析方法，而不是基于高斯系数的参数化模型。假设地磁场的势是一个高斯过程来描述函数的分布。先验相关性由具有非信息性偶极子贡献的显式核函数给出。为了适应历史时期地磁场观测值的非线性特征，我们提出了一种改进的建模策略。首先，只利用那些具有完整地磁场矢量数据的地点，获得对地磁场的粗略估计。然后，该估计用来实现对那些不完整数据的线性化。通过比较过去一千年中的地磁场结果，本文模型与之前的古地磁场模型具有很好的一致性，并且改进了模型的不确定性估计。

ABSTRACT: For the time stationary global geomagnetic field, a new modelling concept is presented. A Bayesian non-parametric approach provides realistic location dependent uncertainty estimates. Modelling related variabilities are dealt with systematically by making little subjective a priori assumptions. Rather than parametrizing the model by Gauss coefficients, a functional analytic approach is applied. The geomagnetic potential is assumed a Gaussian process to describe a distribution over functions. A priori correlations are given by an explicit kernel function with non-informative dipole contribution. A refined modelling strategy is proposed that accommodates non-linearities of archeomagnetic observables: First, a rough field estimate is obtained considering only sites that provide full field vector records. Subsequently, this estimate supports the linearization that incorporates the remaining incomplete records. The comparison of results for the archeomagnetic field over the

past 1000 yr is in general agreement with previous models while improved model uncertainty estimates are provided.
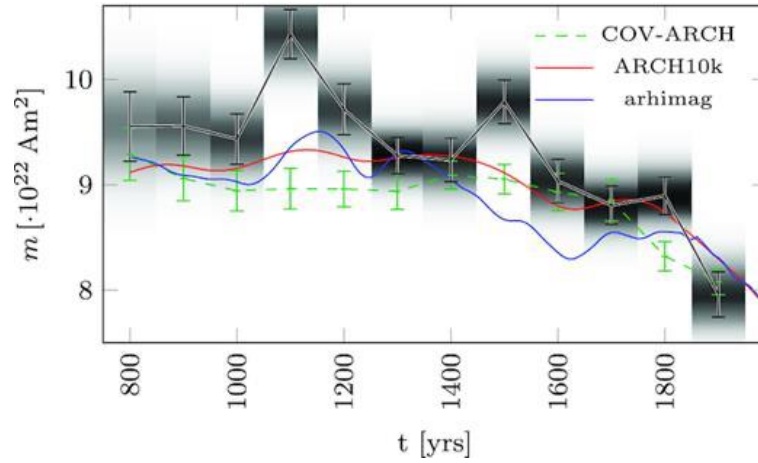

Figure 1. Temporal variation of the dipole moment magnitude based on 10 000 drawn samples. The posterior means are connected by black lines and the error bars indicate one standard deviation. The gray shaded background refers to the kernel density estimate. Results from models COV-ARCH, ARCH10k and arhimag are shown for comparison.
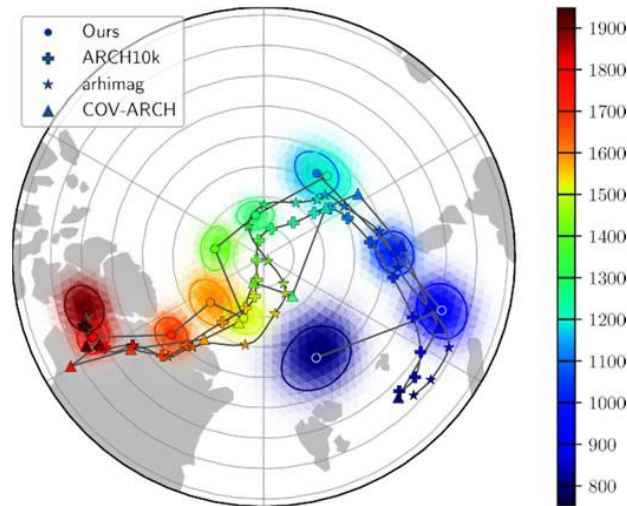

Figure 2. Wander of the geomagnetic north pole. For each epoch in the study, the probability distribution of the location is shown with the mean marked by dots and one sigma marked by an ellipse. The colour varies according to time. For comparison, wander paths for the reference models are shown, without uncertainties in order not to clutter the figure.

26

5. 过去 14 万年德雷克海峡的轨道和千年尺度的南极绕极流变化
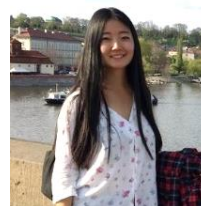
翻译人：张琪 zhangq7@sustech.edu.cn

摘要：南极绕极流在全球海洋环流中起着至关重要的作用，它促进了深水上涌和新水团的形成。在地质时间尺度上，南极绕极流的变化在上个冰期之后就很被约束。此项研究中，我们根据沉积物粒度和地球化学特征，重建了现代极面附近的德雷克海峡中部地区在一个完整的冰期-间冰期（即过去 14 万年）中的 ACC 强度变化。我们发现 ACC 流速在冰期和间冰期之间有明显的变化，冰期海流强度减弱，间冰期的环流更强。叠加在这些轨道尺度的变化上的是高振幅的千年尺度的波动，ACC 强度的最大值与基于硅藻的南极冬季海冰的最小值相关，特别是在盛冰期。作者推断，ACC 与南半球千年尺度的气候振荡密切相关，并通过南极海冰范围的变化得到放大。这些强烈的 ACC 变化通过"冷水路径"调节了太平洋-大西洋的水交换，并可能影响大西洋经向翻转环流和海洋碳储存。

ABSTRACT: The Antarctic Circumpolar Current (ACC) plays a crucial role in global ocean circulation by fostering deep-water upwelling and formation of new water masses. On geological time-scales, ACC variations are poorly constrained beyond the last glacial. Here, we reconstruct changes in ACC strength in the central Drake Passage in vicinity of the modern Polar Front over a complete glacial-interglacial cycle (i.e., the past 140,000 years), based on sediment grain-size and geochemical characteristics. We found significant glacial-interglacial changes of ACC flow speed, with weakened current strength during glacials and a stronger circulation in interglacials. Superimposed on these orbital-scale changes are high-amplitude millennial-scale fluctuations, with ACC strength maxima correlating with diatom-based Antarctic winter sea-ice minima, particularly during full glacial conditions. We infer that the ACC

is closely linked to Southern Hemisphere millennial-scale climate oscillations, amplified through Antarctic sea ice extent changes. These strong ACC variations modulated Pacific-Atlantic water exchange via the "cold water route" and potentially affected the Atlantic Meridional Overturning Circulation and marine carbon storage.
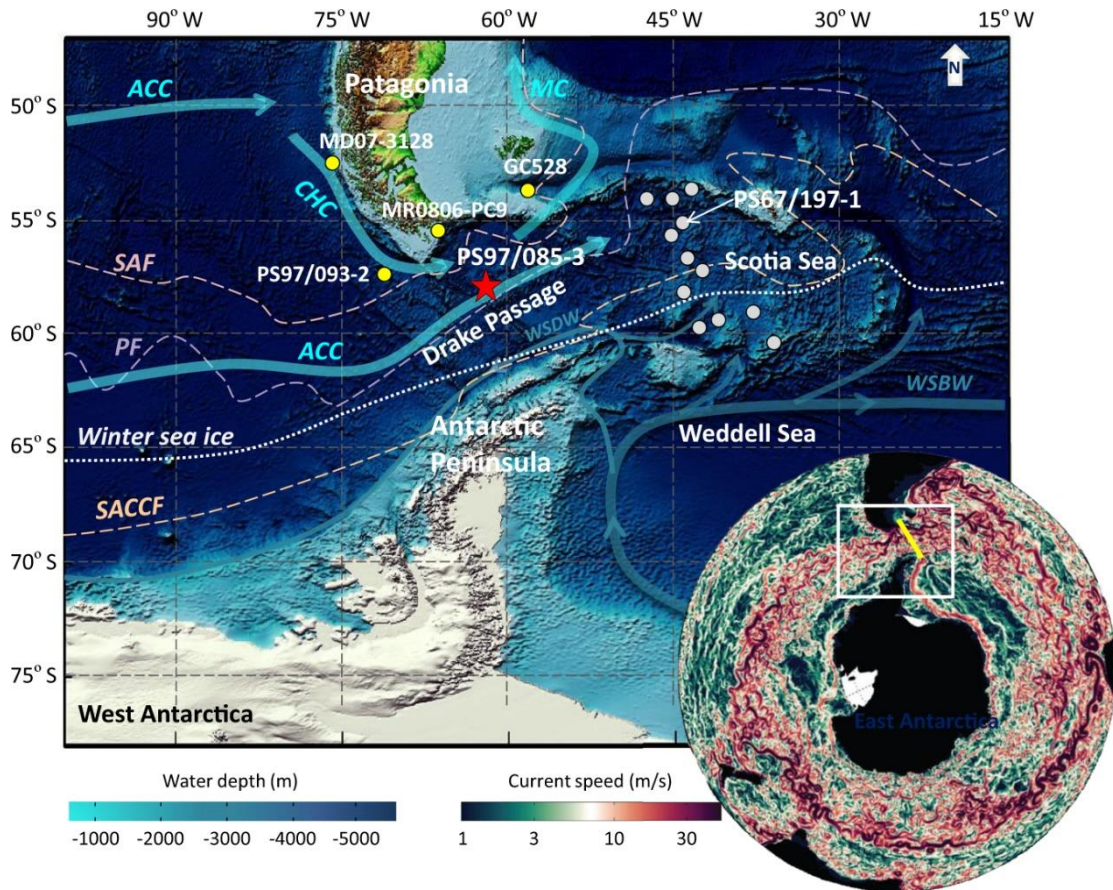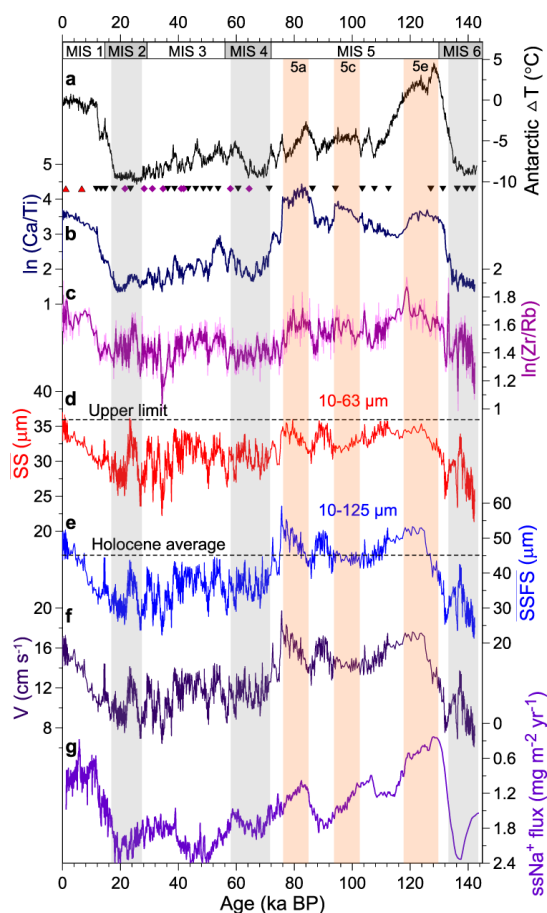

Figure 1. Location map

Figure 2. Reconstructed changes in ACC strength and compared with Antarctic temperature and Southern Ocean sea-ice extent. a) Antarctic temperature changes from the European Project for Ice Coring in Antarctica (EPICA) Dome C ice core[47]. b) High-resolution XRF scanner-derived records of ln(Ca/Ti) (peak area count ratios; black triangles) were applied to fine-tune the Antarctic temperature anomalies together with radiocarbon dates (red triangles), relative paleointensity and paleomagnetic excursions (purple diamonds) age control points from core PS97/085-3. c) XRF-derived ln(Zr/Rb) variations indicate changes in sediment grain-size fractions. d) Mean sortable silt grain size (SS, 10-63 μm) reaches up its upper limit under high flow speeds. e) Mean grain size of sortable silt and fine sand (SSFS, 10-125 μm) was used as the ACC flow speed proxy in this study. f) ACC bottom flow speeds were estimated by the correlation between the SSFS and adjacent current meter data. g) Sea salt sodium (ssNa+) flux from the EPICA Dronning Maud Land (EDML) ice core, a proxy for sea ice extent and atmosphere changes, smoothed with a three-points running mean. Vertical gray bars mark inferred glacial periods and pink bars indicate the sub-interglacial during Marine Isotope Stage (MIS) 5.

6. 碎屑锆石年龄揭示了东海陆架盆地早渐新世以来的长江物源特征

翻译人：刘伟 inewway@163.com

摘要： 长江水系的形成与演化在东亚地区的古地理与古环境演化中起着至关重要的作用。这条中国主要河流的源汇历史为揭示东亚地区由远场和近场板块构造作用驱动的地形梯度的形成提供了信息，并阐明了东海陆架盆地沉积中心的沉降和沉积历史。然而，对东海陆架盆地物源区的研究仍然是一个巨大的挑战。本文基于东海陆架盆地北部渐新统-中新统碎屑锆石 U-Pb 年龄，对不同源区的混合比例进行了统计分析，结果显示了与现代长江相似的锆石年龄分布模式。认为现代长江水系在 ~34 Ma 之前就已经形成，渐新世以来，从扬子克拉通到东海陆架盆地形成了一个东向水系，在中国大陆边缘形成了巨大的沉积体系。蒙特卡罗模型表明，该地区北部渐新世和中新世沉积物主要来自长江、华北克拉通、韩国河流，中新世期间（< 23 Ma），长江水系进一步向南延伸，到达现代台湾的边缘盆地。

ABSTRACT: The origin and evolution of the Yangtze River drainage system play a crucial role in the palaeogeographic and palaeoenvironmental evolution of East Asia. The source-to-sink history of this major Chinese river provides information on the initiation of a topographic gradient in East Asia driven by far-field and near-field effects of plate tectonics and elucidates the subsidence and depositional history of the depocenter in the East China Sea Shelf Basin (ECSSB). Unraveling age constraints on Yangtze provenance, however, remains a big challenge. Here, we review Usingle bond Pb ages of detrital zircon grains from the Oligocene-Miocene successions of the north ECSSB and perform several statistical tests to quantify mixing proportions of different potential source areas that reveal similar age patterns as the modern Yangtze River. We

conclude that the initiation of a modern-type Yangtze drainage was established before ~34 Ma, and confirm that in the Oligocene an eastward drainage system was in place from the Yangtze Craton to the ECSSB where huge depositional systems developed on the Chinese continental margin. Monte Carlo models imply that the Oligocene and Miocene sediments of the north ECSSB were mainly supplied by the Yangtze River and the North China Craton - South Korean rivers, and that during the Miocene (< 23 Ma) the Yangtze drainage system extended further southward, reaching the marginal basins of modern Taiwan.
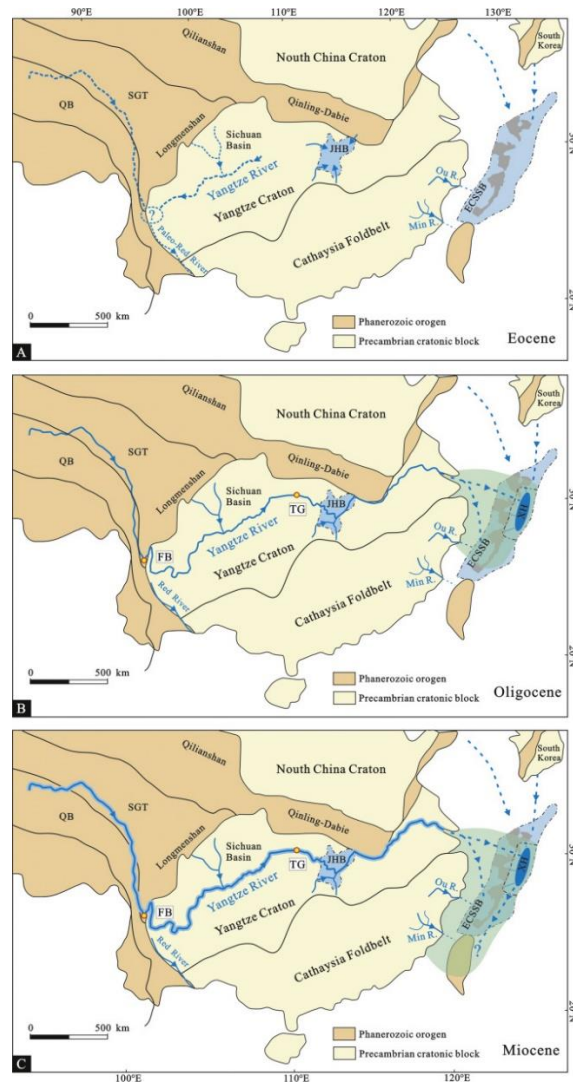

Figure 1. Schematic maps showing the development of the Yangtze River (modified from Zheng et al., 2013a; Zhang et al., 2017; Wang et al., 2018), based on the tectonic framework of China (Zheng et al., 2013b; Zheng, 2015). A) Eocene; B) Oligocene; C) Miocene. ECSSB: East China Sea Shelf

Basin; XH: Xihu Depression; JHB: Jianghan Basin; TG: Three Gorge; SB: Sichuan Basin; FB: First Bend; QB: Qingtang Block; SGT: Songpan-Garze Terrane. The green shade denotes the area of Yangtze River drainage.

7. 全新世以来北大西洋海表水温的变化趋势和百年尺度变化

翻译人：王浩森 11930841@mail.sustech.edu.cn

摘要：本文分析了在冰岛北部（北欧西部）和 Reykjanes 海岭（冰岛盆地）东侧的两个沉积物岩芯，利用高分辨率的烯酮衍生的海面温度（SST）记录研究全新世以来的北大西洋环流变化。冰岛北部的全新世早期的 SST 不稳定（10±1℃）并且比现今高 3℃，这反映了大西洋经向翻转环流（AMOC）向北的热传输过程被间歇性侵入冰岛北部大陆架的极地水所中断。全新世最适期同步发生于 Reykjanes 海岭以东，平均温度为 11.5℃（±0.5℃），与现今相似，并与 AMOC 的持续影响一致。两个记录都表明，在 8000 BP 到 7000 BP 之间，横跨北大西洋的环流加强了。此后，两个海盆地区的 SST 大致反映出了相反的趋势和百年尺度的振荡，以及一次约在 5300 BP 的显着降温事件，与 Bond 4 事件和深水环流的暂时中断相吻合。从 2500 BP 开始，冰岛海盆和北欧西部的海温的分化引起了显着的冷却/变暖偶极子，导致与现今的的温差达到 4.5 ℃。本文研究表明 SST 的变化趋势和拉布拉多及北欧海域的百年尺度上的副极地环流（SPG）及浮冰事件和对流变化相关的变化。

ABSTRACT: Two sediment cores retrieved off North Iceland (western Nordic Seas) and on the eastern flank of Reykjanes Ridge (Iceland Basin) were analyzed to generate high-resolution alkenone-derived sea surface temperature (SST) records to investigate North Atlantic Ocean circulation changes during the Holocene. Early Holocene SSTs off North Iceland were unstable (10 ± 1 °C) and 3 °C warmer than today reflecting active northward heat transport of the Atlantic Meridional Overturning Circulation (AMOC) interrupted by intermittent Polar Waters incursions onto the North Icelandic

shelf. The Holocene thermal optimum occurred synchronously east of Reykjanes Ridge, with a mean value of 11.5 °C (± 0.5 °C) similar to today, consistent with a sustained influence of AMOC. Both records indicate that the circulation across the North Atlantic intensified between 8000 and 7000 yr BP. Thereafter, SSTs in the two basin sites broadly depict opposing trends and centennial-scale oscillations and a notable cooling at ~5300 yr BP that coincides with Bond 4 event and the temporary collapse of the deep-water circulation. From 2500 yr BP onwards, SSTs in the Iceland Basin and the western Nordic Seas diverge leading to a marked cooling/warming dipole resulting in a temperature difference today of 4.5 °C. We show that SST trends and centennial-scale variability reflect variations of the subpolar gyre (SPG) circulation linked to drifting ice events and convection changes in the Labrador and Nordic Seas.
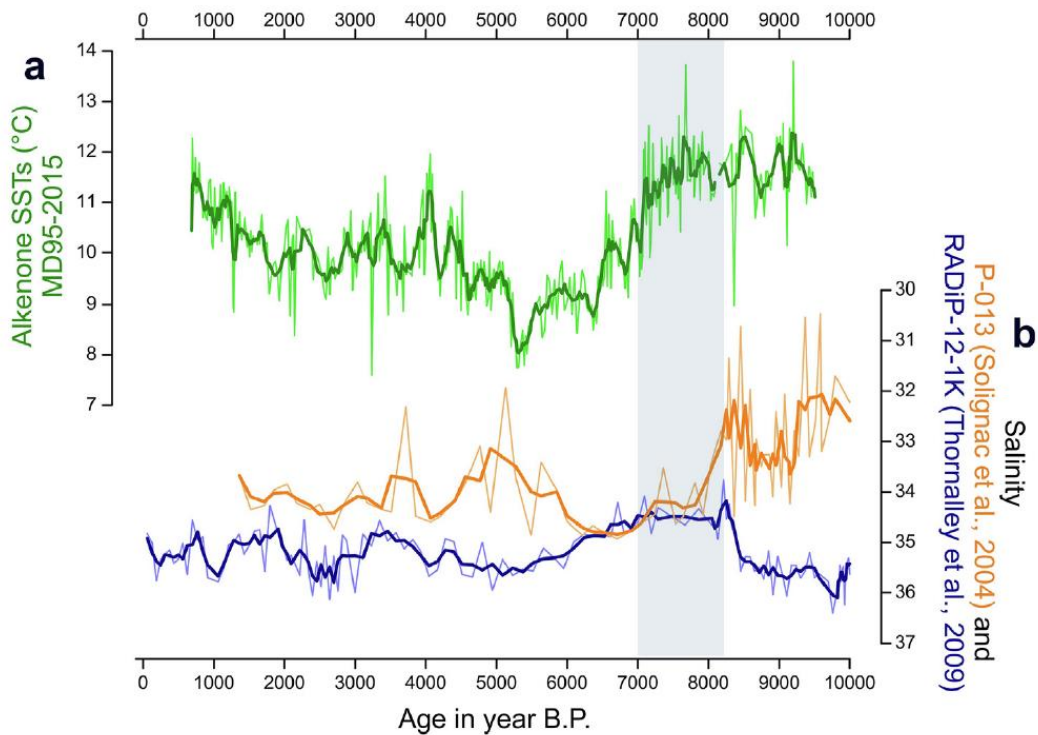

Figure 1. (a) Alkenone-SST reconstruction at the MD95-2015 site (thick green line represents 5 points adjacent-average smoothing, this study). (b) Subsurface salinity reconstruction based on combined Mg/Ca and $\delta^{18}O$ in Globorotalia inflata in the RADiP-12-1K core (dark blue) and sea surface salinity from the P-013 core Greenland Rise, Labrador Sea (orange curve). The thick colored lines in (b) represent 3 points adjacent-average smoothing. The vertical bar highlights the period of SPG activation (8200-7000 yr BP).
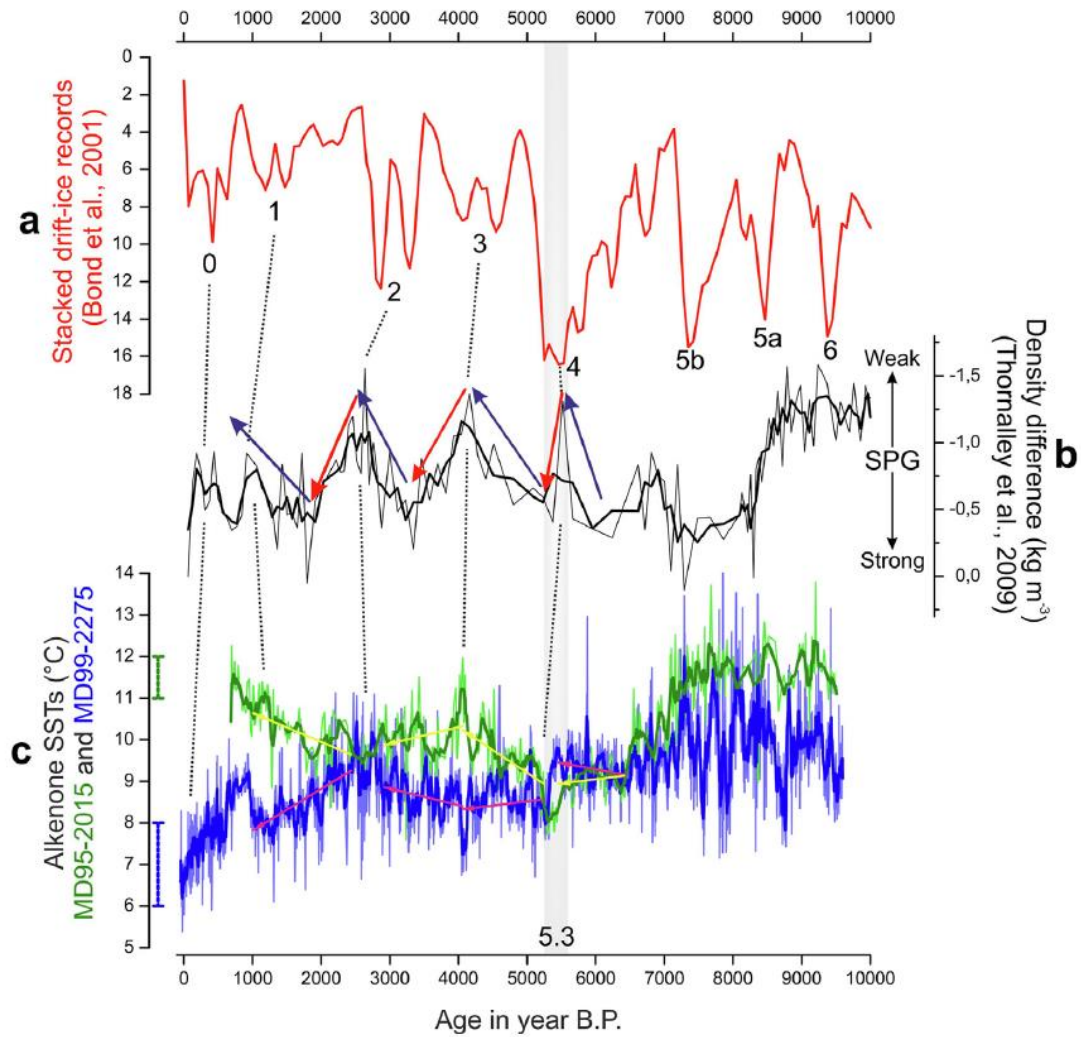
34

Figure 2. (a) Stacked record of the percent hematite stained grains (red curve) and number of each Bond event. (b) Density difference between surface and subsurface waters obtained from paired Mg/Ca and $\delta^{18}O$ in Globigerina bulloides and Globorotalia inflata in core RAPiD-12-1K (Thick line represents 3 points adjacent-average smoothing). Blue and red arrows indicate decreasing and increasing of the SPG circulation, respectively. (c) Alkenone-based SST reconstruction at the MD95-2015 site, East Reykjanes Ridge (green curve) and MD99-2275 site off North Iceland (blue curve). Yellow and magenta arrows on the two curves indicate the trends calculated for selected time-intervals discussed in the text. Blue and green bars next to the Y axis represent the range of modern summer SSTs at the two core sites. The vertical bar highlights the 5.3 event.

8. 冰期终止期北太平洋中层水减弱滞后效应

翻译人：李海 12031330@mail.sustech.edu.cn

摘要：在冰期-间冰期旋回中，北太平洋碳释放主要与北太平洋中层水（NPIW）的形成及其伴随的碳/营养水上升流和生物生产力的变化有关。然而，在间冰期早期 NPIW 与大气 CO_2 变化之间的关系尚不清楚。本文报道了 400 ka 以来西北太平洋 NPIW 演化的高分辨率沉积纪录。指标与模型结果显示，冰期终止后 NPIW 的减弱滞后与中层水盐度降低和北太平洋降雨量增加是同期的。在北太平洋形成这种减弱的 NPIW 可能有助于减弱中-深海分层和降低生物泵净效率从而维持高 CO_2 浓度的大气，阻止南大洋的分层，这将会使间冰期早期大气 CO_2 含量降低。

ABSTRACT: Carbon release from the North Pacific in glacial-interglacial cycles has been mainly linked to the North Pacific Intermediate Water (NPIW) formation and associated carbon/nutrient water upwelling and biological productivity changes. However, relationship between NPIW and atmospheric CO_2 change in the early interglacial remains unclear. Here we report a high-resolution sediment record of NPIW evolution based on paleo-redox changes in the Western North Pacific during the last 400 ka. Our proxy and model results reveal a delayed collapse of NPIW after the glacial termination was coeval with decreased salinity of intermediate water and increased net rainfall in the North Pacific. Such weakened NPIW formation in the North Pacific probably make a contribution to maintain high atmospheric CO_2 concentrations through weakened intermediate-to-deep ocean stratification and reduced subsurface biological pump net efficiency, countering the return to more stratified conditions in the Southern Ocean, which should drive down atmospheric CO_2 during the early interglacial.
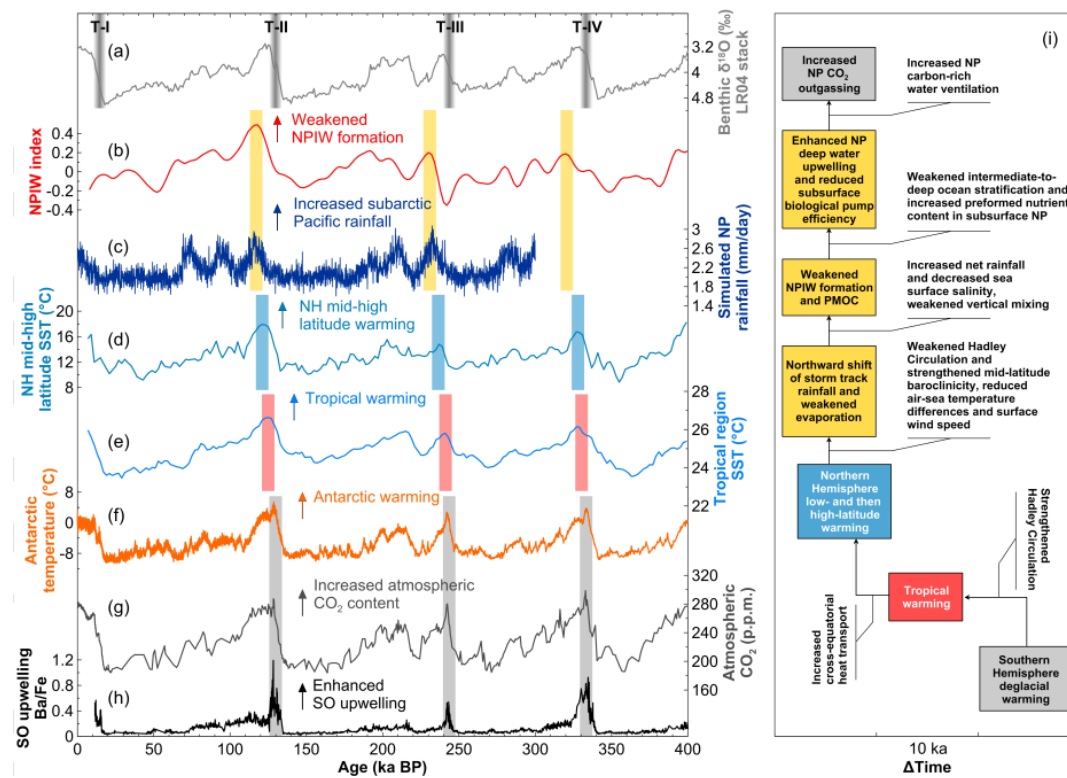
Figure 1. Delayed NPIW collapse compared with the Southern Ocean climate after the glacial termination. (a) LR04 benthic foraminiferal $\delta^{18}O$ stack (Lisiecki and Raymo, 2005). (b) NPIW index. (c) Simulated North Pacific rainfall during the last 300 ka. (d, e) Averaged SSTs of northern Hemisphere mid-high lattitude (Herbert et al., 2001; Lawrence et al., 2009; Sosdian and Rosenthal, 2009) and tropical region (de Garidel-Thoron et al., 2005; Dyez et al., 2016; Herbert et al., 2010; Liu and Herbert, 2004; Medina-Elizalde and Lea, 2005; Russon et al., 2010; Wara et al., 2005) (information of the referenced sites are shown in Table S1). (f) Antarctic temperature (Jouzel and Massondelmotte, 2007). (g) Atmospheric CO_2 concentration (Lüthi et al., 2008). (h) Southern Ocean upwelling index (Jaccard et al., 2013). Vertical bars from (h b) show the steps of climate signal conduction from the Southern Ocean to the North Pacific. Gradient gray vertical bars show the glacial termination 4-1. (i) Flow diagram of the role of NPIW in the global climate surrounding the glacial termination.

37

9. 升温情境下北极层化的加强：上新世中期暖期的证据

翻译人：张亚南 zhangyn3@mail.sustech.edu.cn

摘要：从过去几十年北极大量的海冰融化可以看出该区域是全球变暖表现最为明显的地方。距今 3.264-3.025 百万年前的上新世中期暖期（MPWP），CO_2 水平与现在相似，是理解未来全球变暖影响最接近的类比。来自 Atlantic-Arctic Gateway（AAG）关于相对养分利用率和生产力的高分辨率研究，可以更好的了解过去温暖气候中受分层强度控制的养分有效性。文中，作者利用 ODP Leg 151 在 Fram Strait 采集的沉积物，得到了 MPWP 期间该区域的相对养分利用和生产力的变化。作者发现相对养分利用高（低）表明了暖期（冷期）时分层作用的加强（减弱）。增强的分层抑制了营养物质从中层水向表层的输送，从而导致营养物质更高的利用率。这种现象存在暖期很可能是由夏季海冰融化的加剧和河流输送的增加所导致的结果。因此，淡化的表层可能存储了更多的热量，并进一步加速了海冰融化，这意味着在目前温暖的环境下，更强的分层和上层淡化可能导致北冰洋更多的海冰融化。

ABSTRACT: Global warming is most pronounced in the Arctic as evident from the massive sea ice loss during the past few decades. The Mid-Pliocene Warm Period (MPWP), 3.264-3.025 million years ago with similar CO_2 levels, is the nearest analogue for understanding the impacts of future global warming. High-resolution studies of relative nutrient utilization and productivity from the Atlantic-Arctic Gateway (AAG) can provide insight into the nutrient availability governed by stratification strength during past warm climates. Here, we present relative nutrient utilization and productivity variability during the MPWP using sediments collected during the Ocean

Drilling Program (ODP) Leg 151 from Fram Strait, AAG. We find that the relative nutrient utilization was high (low) implying stronger (weaker) stratification during warm (cold) periods during the MPWP. Stronger stratification inhibits the nutrient influx from intermediate water depths into the surface leading to higher utilization of available nutrients. It existed during warm periods likely due to enhanced summer sea ice melt and river discharge from the hinterland. As a consequence, the freshened surface layer could have stored more heat and accelerated the sea ice melt further implying that in the present-day warm scenario, stronger stratification and upper layer freshening may lead to more sea ice melt in the Arctic Ocean.
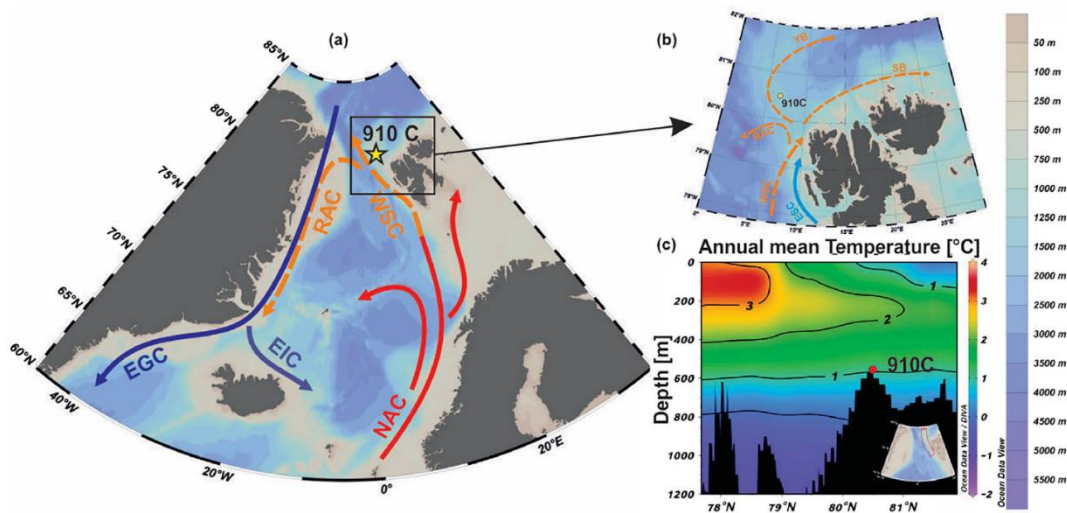

Figure 1. Sampling location. (a) Location of sampling site 910C (80° 15.896′N, 6° 35.430′E) shown as a star. The Norwegian Current transports North Atlantic warm water from 60°N to the Arctic region. RAC-Return Atlantic Current, WSC-West Spitsbergen Current, NAC-North Atlantic Current, EIC-East Icelandic Current, EGC-East Greenland Current. Surface and subsurface water are shown by solid and dotted lines respectively; (b) The warm and saline NAC circulation at the Yermak Plateau. ESC - East Spitsbergen Current, YB-Yermak Branch, SB-Svalbard Branch; (c) Profile of mean annual temperature at the Yermak Plateau; the core location is marked as red dot and the inset shows the transect.
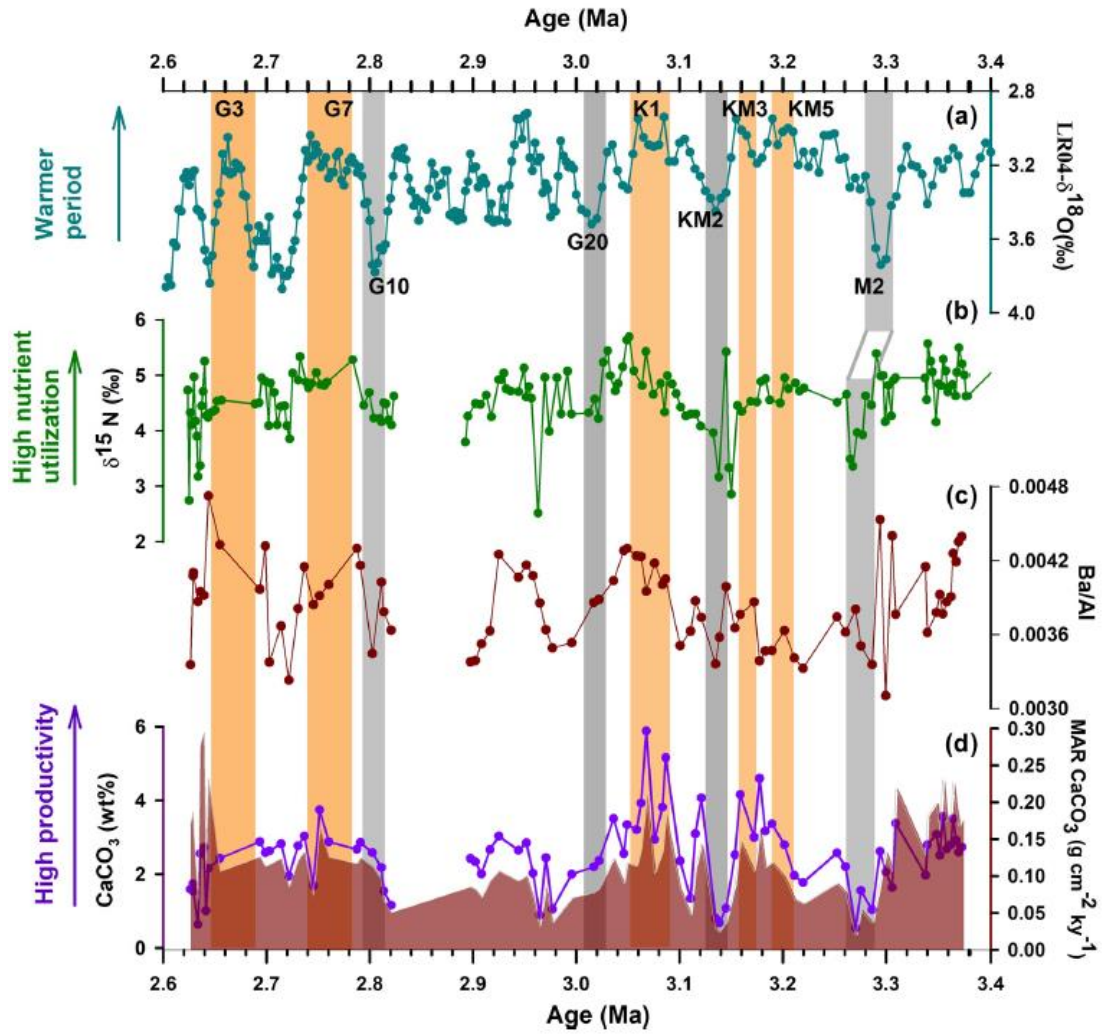
Figure 2. Relative nutrient utilization and productivity variability during late Pliocene. (a) LR04 stack of $\delta^{18}O$ (‰) of benthic foraminifera; (b) $\delta^{15}N$ (‰) representing the relative nutrient utilization during different periods; (c) and (d) Ba/Al, $CaCO_3$ (%) and Mass Accumulation Rate of $CaCO_3$ showing the paleoproductivity variability. Gray bands indicate colder periods while the colored bands show warmer periods. Positions of Marine Isotope Stages M2, KM3, KM2, K1G20, G10, G7, and G3 are shown.
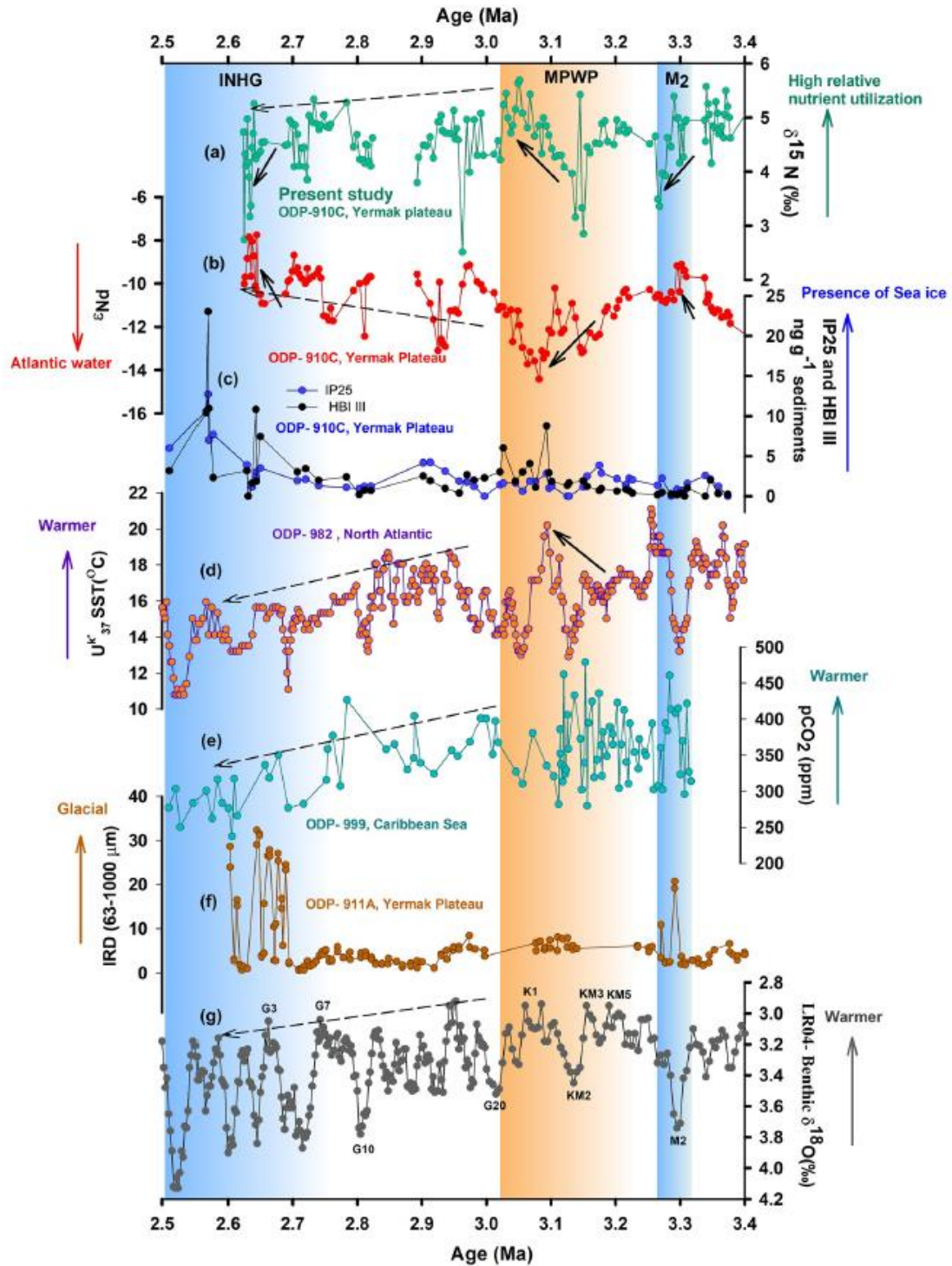
Figure 3. Comparison of relative nutrient utilization with sea surface temperature (SST), Atlantic water inflow, and sea ice extent. (a) $\delta^{15}N$ record from ODP-910C (present study) shows the relative nutrient utilization; (b) and (c) Authigenic εNd record and sea ice proxy (IP25) with open water biomarker Highly Branched Isoprenoid III from 910C; (d) SST record from the ODP Site 982 (North Atlantic) using Alkenone UK37; (e) Atmospheric CO_2 concentration reconstructed using $\delta^{11}B$borate of *G. ruber* from ODP site 999, Caribbean Sea; (f) IRD record from the ODP Site 911A; (g) LR04

stack of $\delta^{18}O$ (‰) of benthic foraminifera. Dashed arrows show long term trend from 3.1 to 2.6 ma and solid arrow indicates glacial-interglacial trends.
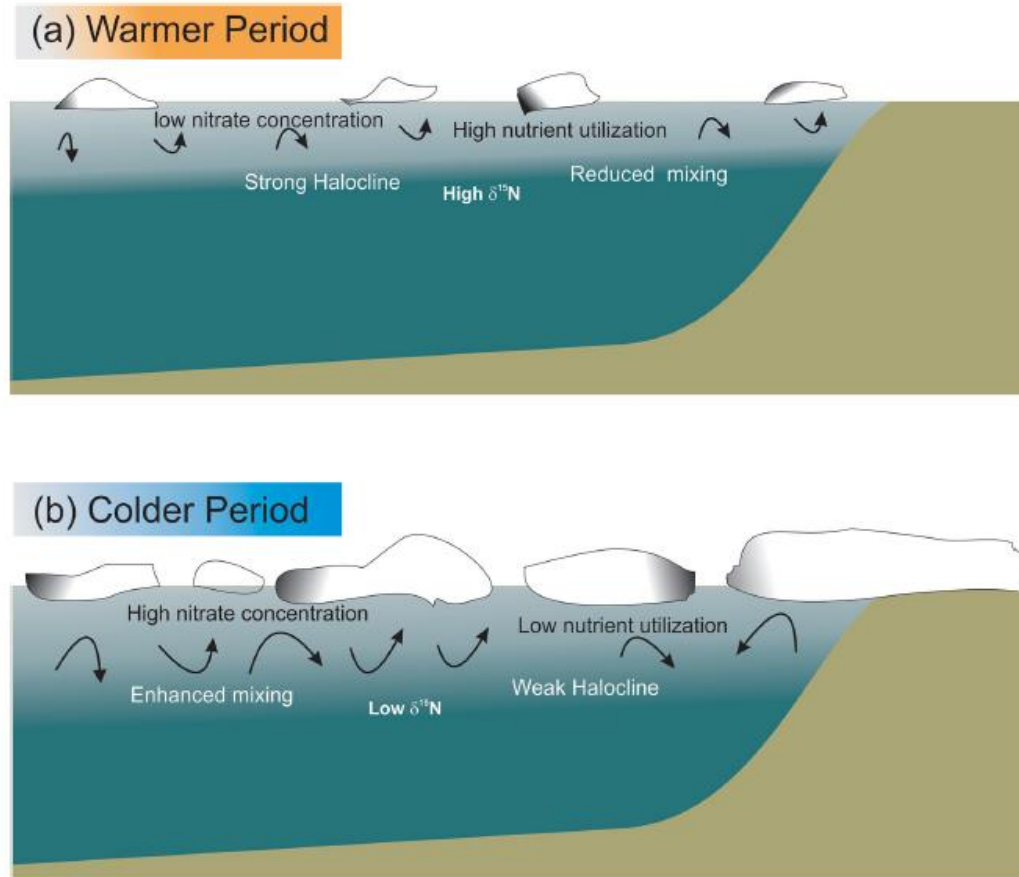

Figure 4. Conceptual representation of stratification at the core site during the late Pliocene. (a) The warmer period is characterized by less sea ice cover at the top (open ocean condition). Fresher surface water is separated from the more saline intermediate water. The reduced mixing is denoted by smaller arrow marks. The stronger stratification inhibits the supply of nutrients to the surface, which results in a high $\delta^{15}N$ value; (b) The colder period is having more sea ice cover at the surface. The brine rejection during the formation of sea ice causes high saline upper surface water. It breaks the stratification formed due to the salinity gradient and causes deeper mixing. Enhanced mixing is represented by bigger arrow marks. It provides nutrients to the surface and which results in a low $\delta^{15}N$ value.

10. Willendorf 考古遗址的黄土磁化率性质：对磁组构同步/后沉积解释的指示

翻译人：郑威 11930589@mail.sustech.edu.cn

摘要： 在 Willendorf 遗址发现了旧石器时代晚期的考古层，与早期奥利尼雅文明有关。这里社会的环境条件，可能与尼安德特人的群体共存，但还未完全了解。本文发表了在 Willendorf 遗址风成黄土的包括磁化率各项异性在内的环境磁学的分析。线状、面状和各向异性程度的数据被用于评估沉积和沉积后的磁组构性质并且推测遗址的环境过程。总而言之，黄土为风成成因，表现出与其他欧洲黄土记录相似的磁性增益和磁组构性质，但不同于很多"干燥"黄土点位，磁性矿物学显示在加热过程中表现出更高的磁化率。我们推断，由于有机物的存在，在加热过程中新生成了磁铁矿。从表面上看，磁化率各向异性的性质与以往的研究是一致的，表明了这是纯风成黄土，叠瓦状则表明沉积后的斜坡运动朝向多瑙河方向，这使得了古风向的推断难以解释。这些沉积后的磁性组构变化很可能发生在其他具有相似地貌环境的地点。

ABSTRACT: At the Willendorf site Upper Paleolithic archeological layers associated to early Aurignacian cultures were found. The environmental conditions of the associated society, potentially co-existing with Neanderthal groups, is still not fully understood. Here, we report on environmental magnetic analyses including anisotropy of the magnetic susceptibility (AMS) carried out on loessic aeolian sediments at the Willendorf site. Data on lineation, foliation and the degree of anisotropy were used to assess depositional and post-depositional magnetic fabric properties and to deduce site-specific environmental processes. Overall, the loess is of aeolian origin and shows magnetic enhancement and magnetic fabric properties similar to those of other

European loess geoarchives, but the magnetic mineralogy differs from many 'dry' loess sites, insofar as it shows a higher susceptibility during heating. We infer an enhanced neoformation of magnetite during heating due to the presence of organic matter. While at face value the AMS properties are indicative of pure aeolian loess consistent with previous studies, imbrication suggests post-depositional slope movement toward the Danube, which obscures inferences on palaeo-wind direction. It is well possible that these post-depositional magnetic fabric alterations occur at other localities with similar geomorphological settings.
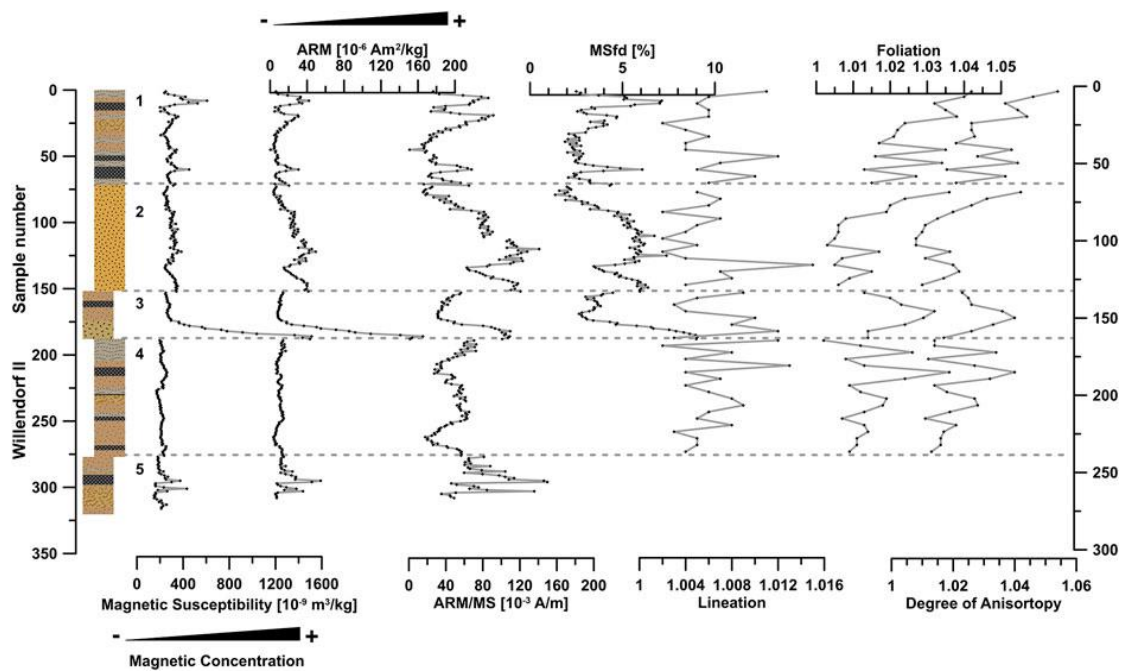

Figure 1. Rock magnetic parameters for the five profiles (from Figure 2; plotted on top of each other against lithology on the left), and their interpretation regarding magnetic concentration and grain size for the magnetic susceptibility (MS), anhysteretic remeanent magnetisation (ARM) and the ARM/MS ratio. The frequency dependent magnetic susceptibility ($\chi_{fd\%}$) may be regarded as representing a combination of magnetic concentration and grain size. Note that the ordinate is not representing a continuous stratigraphy.